Cell Reports

Article

Top-down feedback enables flexible coding strategies in the olfactory cortex

Graphical abstract

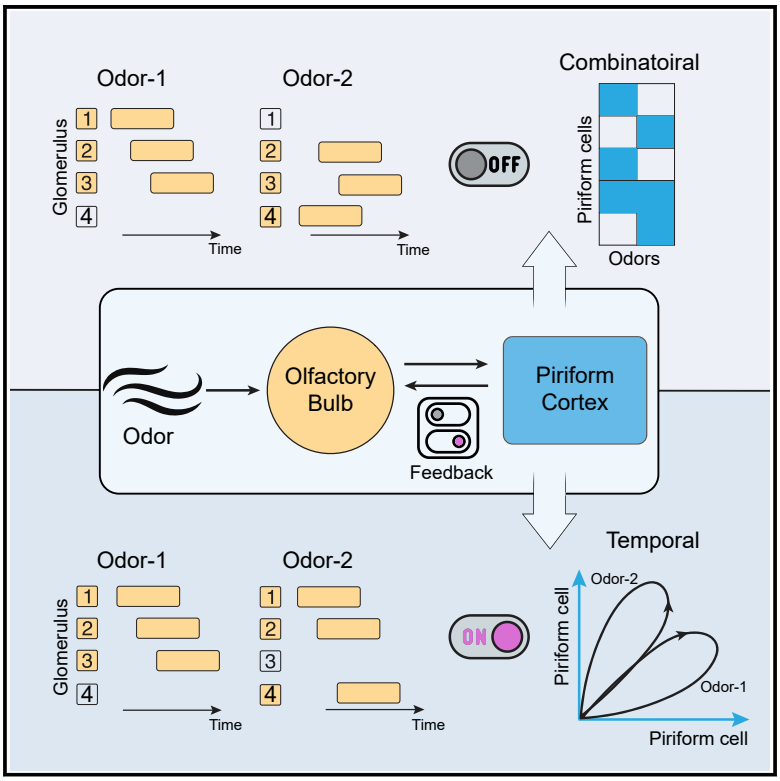

Authors

Zhen Chen, Krishnan Padmanabhan

Correspondence

krishnan_padmanabhan@urmc.rochester.edu

In brief

Chen and Padmanabhan show that centrifugal feedback in the early olfactory system shapes the temporal structure of neural activity in the olfactory cortex. This allows flexible coding strategies by which to represent odor information in the olfactory cortex that improving behavioral performance in odor discrimination tasks.

Highlights

- Feedback shapes temporal structure of piriform cortical cell activity
- Feedback controls information to piriform cortex by restructuring bulb output
- Feedback reshapes cortical representation of glomerular activation pattern
- Feedback improves behavioral performance in odor discrimination task

Chen & Padmanabhan, 2022, Cell Reports *38*, 110545
March 22, 2022
https://doi.org/10.1016/j.celrep.2022.110545

CellPress

Cell Reports

CellPress
OPEN ACCESS

Article

Top-down feedback enables flexible coding strategies in the olfactory cortex

Zhen Chen[1] and Krishnan Padmanabhan[2,3,*]
[1]Department of Brain and Cognitive Sciences, University of Rochester, Rochester, NY 14627, USA
[2]Department of Neuroscience, Neuroscience Graduate Program, Del Monte Institute for Neuroscience, Center for Visual Sciences, Intellectual and Developmental Disability Research Center, University of Rochester School of Medicine and Dentistry, Rochester, NY 14642, USA
[3]Lead contact
*Correspondence: krishnan_padmanabhan@urmc.rochester.edu
https://doi.org/10.1016/j.celrep.2022.110545

SUMMARY

In chemical sensation, multiple models have been proposed to explain how odors are represented in the olfactory cortex. One hypothesis is that the combinatorial identity of active neurons within sniff-related time windows is critical, whereas another model proposes that it is the temporal structure of neural activity that is essential for encoding odor information. We find that top-down feedback to the main olfactory bulb dictates the information transmitted to the piriform cortex and switches between these coding strategies. Using a detailed network model, we demonstrate that feedback control of inhibition influences the excitation-inhibition balance in mitral cells, restructuring the dynamics of piriform cortical cells. This results in performance improvement in odor discrimination tasks. These findings present a framework for early olfactory computation, where top-down feedback to the bulb flexibly shapes the temporal structure of neural activity in the piriform cortex, allowing the early olfactory system to dynamically switch between two distinct coding models.

INTRODUCTION

An open question in neuroscience is which aspects of neural activity convey stimulus information and how neurons at later processing stages read out this information. In olfaction, one model of neural coding posits that temporal patterns of activity in principal neurons in the main olfactory bulb (MOB) are relayed to the olfactory cortex, and this timing is critical for odor representation (Chong and Rinberg, 2018; Haddad et al., 2013; Laurent, 2002). Another model proposes that these temporal patterns from the MOB are transformed into combinatorial patterns of activity in the cortex (Bolding and Franks, 2017; Stern et al., 2018; Stettler and Axel, 2009). Each model has experimental support and draws on theoretical frameworks, but it remains unclear how these models relate to different behaviors and the extent to which they are instantiations of a single framework of computing.

Olfactory coding is most often studied in early olfactory circuits. Volatile molecules bind to olfactory receptor neurons (ORNs) in the nasal epithelium. ORNs encode the identity and concentration of monomolecular odorants (Buck and Axel, 1991; Malnic et al., 1999). ORN axons converge onto one to two neuropil structures, called glomeruli, in the MOB (Mombaerts et al., 1996). Mitral/tufted (M/T) cells in the MOB receive direct excitatory input from ORNs and relay odor information to cortical regions. Each odorant activates a subset of glomeruli with different onset latencies, which, in turn, gives rise to odor-specific patterns of M/T cells (Bathellier et al., 2008; Cury and Uchida, 2010; Paoli et al., 2018; Spors and Grinvald, 2002). Thus, ensembles of M/T cells vary in the identity (which cells fire) and timing (when they fire) of their activity (Gire et al., 2013a; Uchida et al., 2014).

Sniffing acts as a metronome organizing the timing of these M/T responses (Bathellier et al., 2008; Shusterman et al., 2011). Although M/T cell activity can occur throughout the sniff cycle, studies have shown that piriform cortical cells respond within narrower windows of activity after onset of inhalation (Bolding and Franks, 2017; Miura et al., 2012). This timing is controlled by intracortical inhibition, which suppresses the activity of piriform cortical cells following activation of the earliest glomeruli. Consequently, studies suggest that piriform cortical cells are less sensitive to M/T cell input from glomeruli activated later in the sniff (Bolding and Franks, 2017; Miura et al., 2012; Stern et al., 2018). The pattern of activated piriform cells is sufficient to represent odor identity (Bolding and Franks, 2017; Gire et al., 2013b), suggesting that odor information encoded in the temporal structure of M/T cell activity is transformed into a combinatorial code.

Physiological and behavioral studies show that animals have access to the temporal information in glomerular patterns that would be lost if only a combinatorial code was used. In mice expressing channelrhodopsin-2 in ORNs, varying the stimulation timing of two spots corresponding to different glomeruli triggers different responses in the identity and timing of piriform cortical cells (Haddad et al., 2013). Mice can report these differences in the relative timing of glomerular activation (Ackels et al., 2021; Chong et al., 2020; Rebello et al., 2014; Smear et al., 2011).

Thus, information encoded in the temporal structure of glomerular activity is available to guide behaviors, but it is unclear how olfactory circuits access this information.

One clue is that studies on olfactory coding focus largely on the feedforward projections from the MOB to the piriform cortex. However, cells in the bulb receive major centrifugal or feedback inputs from the piriform cortex (Boyd et al., 2012; Otazu et al., 2015; Padmanabhan et al., 2019; Shipley and Adamek, 1984). Could different findings regarding how the piriform cortex codes for odor information be reconciled by examining the role of feedback from the piriform cortex to the bulb? We tested this in a spiking network model that recapitulated the circuit structure within and between the MOB and piriform cortex. Differences in feedback activity determined how much odor information was conveyed by the temporal patterns of MOB input.

Our results show that feedback allows differences in the timing and identity of glomerular activation to be encoded in the temporal patterns of piriform cortical cells. This information improved behavioral performance in an odor discrimination task. We propose that feedback serves to flexibly sculpt the temporal organization of piriform cell activity, changing between combinatorial and temporal codes, and hypothesize that the amount of feedback arises from differences in the animal's internal state (arousal, attention, etc.), learning, and memory.

RESULTS

Odors activate distinct spatiotemporal patterns of glomeruli

To understand the functional role of feedback from the piriform cortex (PCx) to the MOB in olfactory coding, we built a spiking neuronal network model that recapitulated the circuit architecture of the MOB and PCx (Figure 1A; STAR Methods). Our model captured essential features of the olfactory system's architecture and the biophysical properties of all cells throughout the circuit. A schematic of the network architecture is shown in Figure 1A (STAR Methods; Figure S1 network parameters are summarized in Tables S1 and S2).

Next, we defined an ethologically and behaviorally relevant time window corresponding to a single sniff to study the dynamics of our network (Rinberg et al., 2006; Uchida and Mainen, 2003; Wesson et al., 2008). Model odors presented during a 250-ms window (4-Hz sniff) were designed to match the activation patterns of glomeruli by odorants in terms of identity (5%–20% of all glomeruli) and timing (different onset latencies and durations) (Fantana et al., 2008; Gschwend et al., 2016; Vincis et al., 2012). All M/T cells associated with a stimulated glomerulus received correlated ORN input that decayed over time (Figures 1B and S2). The earliest glomerulus was the strongest at driving M/T cells, consistent with previous studies (Johnson and Leon, 2007; Soucy et al., 2009; Wachowiak and Cohen, 2001). Odors were thus defined by the pattern of the activated glomeruli (identity) and their onset latencies (timing) (Figures 1C1 and 1D1), recapitulating the glomerular responses to natural odors (Meister and Bonhoeffer, 2001; Rubin and Katz, 1999). For example, the two odors in Figure 1B differed in the identity of the earliest glomerulus as well as the timing of the third glomerulus. We generated 300 model odors, and although most odor pairs (>80%) were weakly anti-correlated because of the sparseness of glomerular activation, we had numerous examples of strongly correlated odor pairs (Figures 1C2 and 1D2) spanned a range of −0.1 to 0.9 (Figures 1C3 and 1D3; n = 44,850).

Feedback modulates the output of the MOB via granule cells

Studies have shown that feedback can affect olfactory bulb activity via the granule cell population (Boyd et al., 2012; Markopoulos et al., 2012). To study the functional role of feedback, we modeled an inactivation experiment by simulating the dynamics of MOB neurons when the centrifugal synaptic weights to granule cells (GCs) were set to zero (feedback OFF) versus when feedback from the PCx corresponded to weights measured in experiments (feedback ON). Because only the top-down connections from the PCx to the MOB were silenced, all other network connectivity was preserved.

In response to a model odor (odor 1; Figure 1B), the M/T cell population firing rate increased transiently after activation of the earliest glomerulus (Figure 2A1, bottom) and then decayed because of firing of inhibitory GCs (Figure 2A2) when feedback was OFF. With feedback ON, however, the M/T cell population fired persistently (Figure 2B1, bottom; Figure S2) despite the overall increase in GC activity (Figure 2B2). Because our results reflected the activity of the entire M/T cell population in the network, we randomly sampled M/T cells ($n = 9$ cells per sampling; STAR Methods) to relate our finding to experimental results from single-unit studies. Consistent with previous work (Bolding and Franks, 2018), the kinetics of single-unit M/T cells were similar for feedback OFF and ON (Figure 2E). An exponential function (STAR Methods) fit to the decay of the sampled M/T cell firing rates from the peak to the end of the sniff showed that the time constants for feedback OFF were not significantly different from that for feedback ON ($n = 300$ odors; Figure 2E3). Some M/T cells were enhanced by feedback throughout a sniff cycle, whereas other M/T cells were largely suppressed (Figures 2A1 and 2B1, top). M/T cells driven by odor-activated glomeruli were mostly enhanced by feedback (Figure S3). When glomerular activation was sparse and feedback was OFF, a large number of M/T cells fired spontaneously, laterally inhibiting odor-driven M/T cells via GCs. Turning feedback ON suppressed these spontaneously active M/T cells, leading to disinhibition of odor-driven M/T cells. When more glomeruli were activated by the model odors (Figure 2F), we found suppression and enhancement of odor-driven M/T cells (Figures 2G1–2G3). Cells with a firing rate of less than 20 spikes *(spks)/s* were largely suppressed by feedback ($p < 0.001$, Wilcoxon signed-rank test), consistent with previous findings (Boyd et al., 2012). However, for M/T cells with higher firing rates (not reported in Boyd et al., 2012), our model predicted that their responses would be enhanced by feedback. The effect of feedback on M/T activity thus depended on the number of activated glomeruli; this was not surprising because differences in glomerular activation patterns vary depending on odor identity and concentration.

Next, to dissect the synaptic input contributing to the dynamics of the network (Nelson and Valakh, 2015), we plotted the voltages and various synaptic inputs for two M/T cells (Figures 3A1 and 3B1). The example cell receiving glomerular input

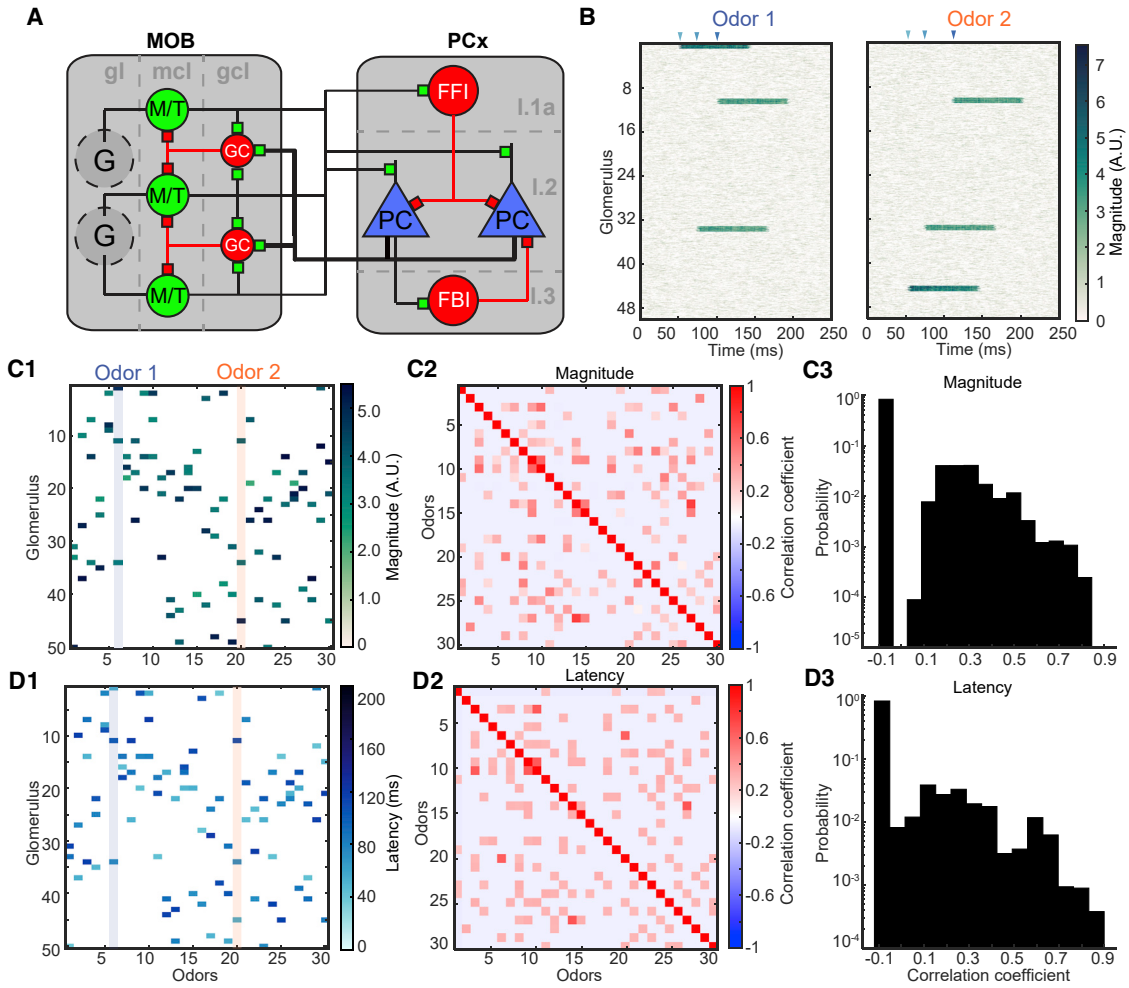

Figure 1. Spiking network schematics and odor definition

(A) Schematics of the MOB-PCx network. In the main olfactory bulb (MOB), glomeruli (G) in the glomerular layer (GL) relay sensory information to mitral/tufted (M/T) cells in the mitral cell layer (mcl). M/T cells receive inhibition from granule cells (GCs) in GC layer (GCL). In the piriform cortex (PCx), piriform cortical (PC) neurons in layer 2 (l.2) and feedforward inhibitory (FFI) neurons in superficial layer (l.1) receive direct feedforward excitation from the MOB. Local inhibitory neurons (FBI) in the deeper layer (l.3) provide feedback inhibition of PC cells. Excitatory synapses are shown in green and inhibitory synapses in red. Recurrent connections between cells of the same type are omitted for clarity. The thick connecting lines from PC cells to GCs correspond to feedback from the PCx to the MOB.

(B) Glomerular input patterns for two odors. The color bar indicates the magnitude of glomerular input. The triangles on top indicate activation of the three glomeruli. Left, odor 1: G1, 52 ms; G2, 74 ms; G3, 101 ms. Right, odor 2: G1, 52 ms; G2, 74 ms; G3, 110 ms.

(C) Magnitude of glomerular input for 30 example odors across 50 glomeruli.

(C1) Each column corresponds to an odor, and the two highlighted ones correspond to the two odors shown in (B).

(C2) Pairwise correlation of magnitude between different odors.

(C3) Histogram of the pairwise correlation of magnitude across all odor pairs (n = 44,850 pairs).

(D) Similar to (C) but for glomerular timing of each odor.

(M/T 1) only fired transiently in the early phase of the glomerular input for feedback OFF but fired throughout glomerular activation when feedback was ON. In contrast, the cell not receiving glomerular input (M/T 2) fired spontaneously when feedback was OFF but was silenced when feedback was ON. A different model odor would activate a different subset of glomeruli, with different subsets of M/T cells enhanced and suppressed by feedback. To understand the effect of feedback on M/T cells across all odors, we compared the odor-evoked responses of each cell between feedback ON and OFF (Figures 2C and S3). The feedback-induced changes in M/T firing rates were bimodally distributed. Feedback increased the signal-to-noise ratio of the MOB output by selectively enhancing the firing of M/T cells driven by odor-activated glomeruli and suppressing the activity of M/T cells not connected to stimulated glomeruli.

We found that, similar to M/T cells, feedback resulted in enhancement and suppression of firing rates in GCs (Figures 2D and S3) even though all centrifugal inputs were excitatory. Suppression of GCs by feedback arose from disynaptic inhibition between GCs (Figures 3A2 and 3B2). One major source of

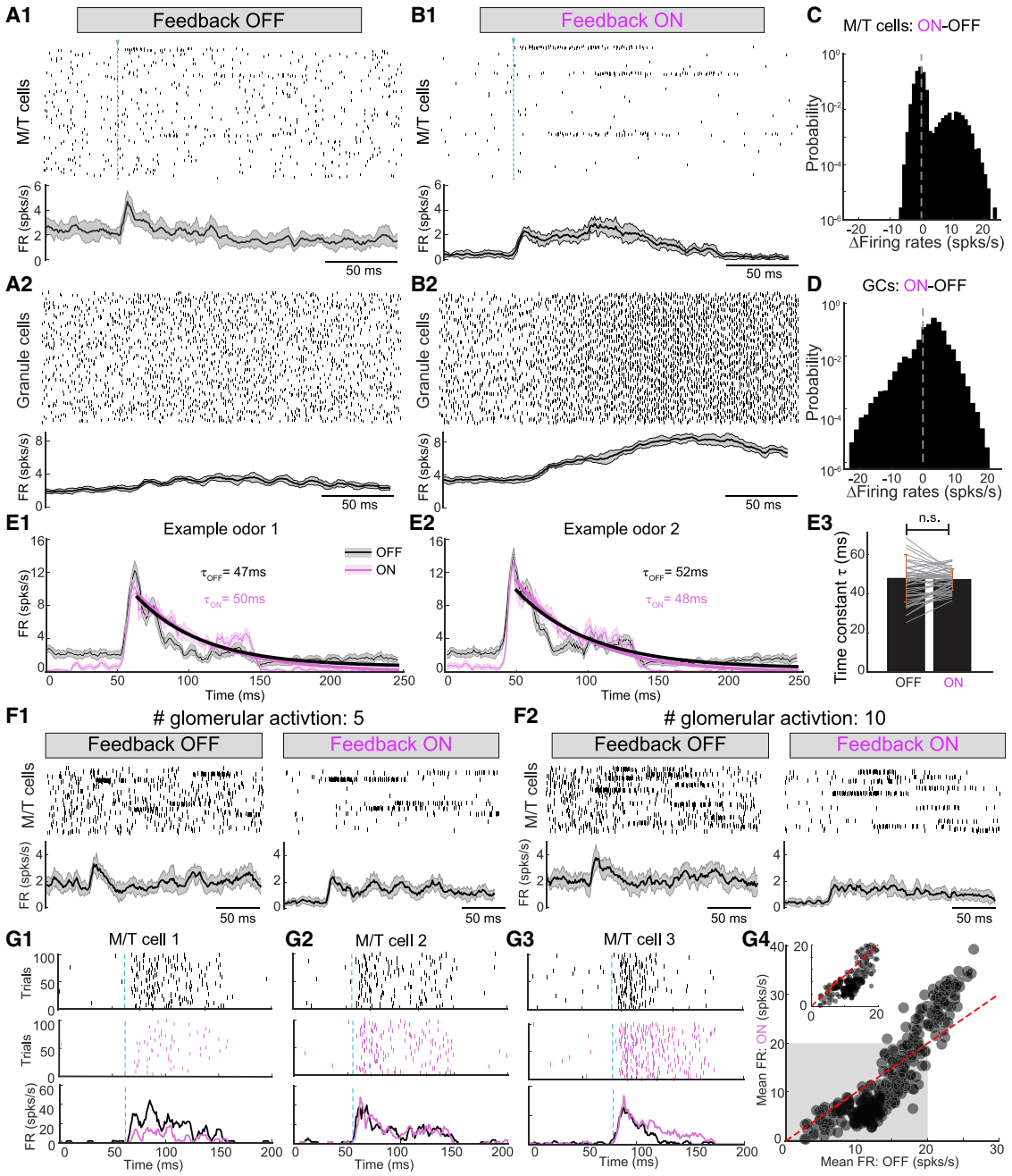

Figure 2. Feedback modulates M/T cell firing by controlling the GC population

(A) MOB cell responses to an odor with feedback OFF.

(A1) Raster plot of M/T cells in one trial (top). Each row corresponds to the spike train of one M/T cell. Each tick mark represents a spike. The blue dashed line indicates activation of the earliest glomerulus for the odor. Bottom: population firing rate of all M/T cells (mean ± SD, $n = 10$ trials).

(A2) Similar to (A1) but for GCs.

(B) Similar to (A) but for feedback ON. Three groups of M/T cells driven by odor-activated glomeruli fire persistently throughout a sniff, whereas others only fire sparsely.

(C) Histogram of the feedback-induced changes in the firing rates of M/T cells (n = 1250) across all model odors (n = 300). Positive values of the firing rate change signify enhancement by feedback, and negative values signify suppression.

(D) Similar to (C) but for GCs. GCs are enhanced and suppressed by changes in feedback.

(E) Firing rate kinetics of randomly sampled M/T cells ($n = 9$ cells per sampling repeat) from the entire M/T cell population for feedback OFF and ON.

(E1 and E2) Population firing rate of randomly sampled M/T cells to two example odors. Thick lines are exponential fits to decay from peak to end of a sniff (mean ± SD, n = 20 repeats). The time constants of exponential decay are indicated.

(legend continued on next page)

this disynaptic inhibition could be deep short-axon cells (dSACs) which, compared with GCs, receive a higher convergence and stronger excitatory drive from the PCx (Boyd et al., 2012). dSACs also receive inputs from M/T cells and provide feedforward inhibition to GCs (Burton and Urban, 2015). In our network, the heterogeneous parameters used for GCs covered a diversity of biophysical properties (STAR Methods), including GCs and dSACs in the GC layer (GCL). For example, GC-1, receiving stronger top-down feedback, was more like a dSAC and, thus, enhanced by feedback, whereas GC-2, receiving less top-down feedback, was more like a GC and, thus, suppressed (Figures 3A2 and 3B2), consistent with the heterogeneity in the feedback among GC population observed previously (Otazu et al., 2015).

Balance between excitatory and inhibitory inputs is essential for stabilizing the dynamics of a network (Chen and Padmanabhan, 2020; Ozeki et al., 2009). We found that feedback played a role in stabilizing this balance. To quantify this, we calculated the ratio of excitatory and inhibitory synaptic inputs for each cell (Figures 3C and 3D). Positive values indicated that a cell's subthreshold membrane dynamics were dominated by excitation, whereas negative values corresponded to a net inhibitory drive, with zero corresponding to a balance of the two. When feedback was OFF, weak inhibition dominated M/T cells and excitation dominated GCs (Figure 3C). However, when feedback was ON, the synaptic drive to M/T cells and GCs became bimodally distributed (Figure 3D). A large proportion of M/T cells became dominated by strong inhibition, with a small population slightly excited (Figure S3). Similarly, one subpopulation of GCs was dominated by excitation and the other by inhibition, illustrating the subdivision of functionally distinct GC subpopulations on which top-down feedback had a different net effect. Feedback therefore balanced excitatory and inhibitory drive across the network. As a result, although M/T cells formed distributive connections with GCs, feedback from the PCx revealed functionally distinct subpopulations of local inhibitory interneurons differentially sensitive to the ratio of excitatory to inhibitory inputs (E/I).

Feedback controls the temporal dynamics of the PCx, leading to a circuit that is critical for pattern separation

The PCx has been shown to be essential for integrating odor information from individual glomeruli to form odor percepts (Gottfried, 2010; Miura et al., 2012; Stettler and Axel, 2009) and has a critical role in guiding behaviors (Choi et al., 2011). We next wanted to know how restructuring the dynamics of M/T cells by changing feedback affects the dynamics of the PCx.

First, when feedback was OFF, piriform cortical (PC) cells increased their population firing rates, peaking ~16 ms after activation of the earliest glomerulus (Figure 4A). This activity was sharply truncated by local feedback inhibitory (FBI) cells, which were recruited within the PCx (Stern et al., 2018), and consistent with the model where temporal to combinatorial remapping of the neural representations of odors occurs from the MOB to the PCx. When feedback was ON, however, PC cells fired throughout the sniff cycle, including over activation of multiple, temporally staggered glomeruli (Figure 4B). When the centrifugal input to the bulb was ON, FBI cells in the PCx were recruited only sparsely, no longer truncating the activity of PC cells (Figure S4). This was due to the sparser M/T cell input that drove sparser populations of PC cells (Figure 4A, center, purple dashed curve). Across activation of 3, 5, or 10 glomeruli, feedback to the MOB resulted in persistent and prolonged firing in PC cells (Figures 4C and D1; $n = 300$ odors). These results suggested that feedback gated the temporal structure of neural activity in the PCx, across different levels of M/T sparsity. The temporal structure of PC cells was abolished when we activated all glomeruli in our model (Figure S5), consistent with experiments that use wide-field optogenetic stimulations to drive all glomeruli on the dorsal surface (Bolding and Franks, 2018). Stimulating all glomeruli resulted in recruitment of a large population of FBIs, which truncated the firing of PC cells even when feedback was ON. Finally, the temporal structure of M/T cell activity was driven by differences in the number, identity, and timing of glomerular activation. These dynamics were due to complex network-level interactions because simply increasing the spontaneous activity of GCs under the feedback OFF condition did not result in the persistent dynamics of PC cells as feedback (Figure S5).

We next studied the dynamics of PCx activity for each odor with three quantities that captured the overall temporal structure of the population: the peak firing rate, the delay between the peak and the activation time of the earliest glomerulus, and the decay rate from the peak to the baseline firing rate (Figure 4D2). With feedback ON, the peak firing rate of PC cells decreased significantly (Figure 4E1) because of a smaller subset of cells responding to odor presentation. However, activity across this sparser population persisted longer with smaller decay rates (Figure 4E2) and a reduced response latency relative to the earliest glomerulus that was activated (Figure 4E3, bottom). These effects arose from the information relayed from the bulb to the PCx because feedback had no significant effect on the response latency of M/T cells receiving input from the glomeruli (Figure 4E3, top).

These results only tell us that feedback can alter the dynamics of activity in the PCx, leaving open whether such differences are actually relevant for the coding of odor information. To address this question, we used an odor discrimination task where an

(E3) Time constants of exponential decay for all odors (n = 300 odors, p > 0.05, Wilcoxon signed-rank test). Lines correspond to 50 example odors pairs.
(F) M/T cell responses vary with the number of glomeruli that are activated.
(F1) The odor sequentially activates 5 glomeruli. Top: raster plot of M/T cells in one trial. Bottom: population firing rate of all M/T cells (mean ± SD, n = 10 trials).
(F2) Same as (F1) but for an odor activating 10 glomeruli.
(G) Feedback ON has diverse effects on M/T cell responses to odors.
(G1–G3) Odor-evoked responses when 10 glomeruli are activated for three example M/T cells that are modulated differently by feedback. M/T 1, suppressed; M/T 2, neutral; M/T 3, enhanced. Top: raster plot of spikes across 100 trials for feedback OFF. Center: raster plot of spikes across 100 trials for feedback ON. Bottom: trial-averaged firing rate of the cell.
(G4) Scatterplot of the mean M/T firing rate averaged across trials for the duration of glomerular activation. Inset: magnification of the shaded area of less than 20 spks/s shows that M/T cell responses are largely suppressed when feedback is ON. The red dashed line is the identity line.

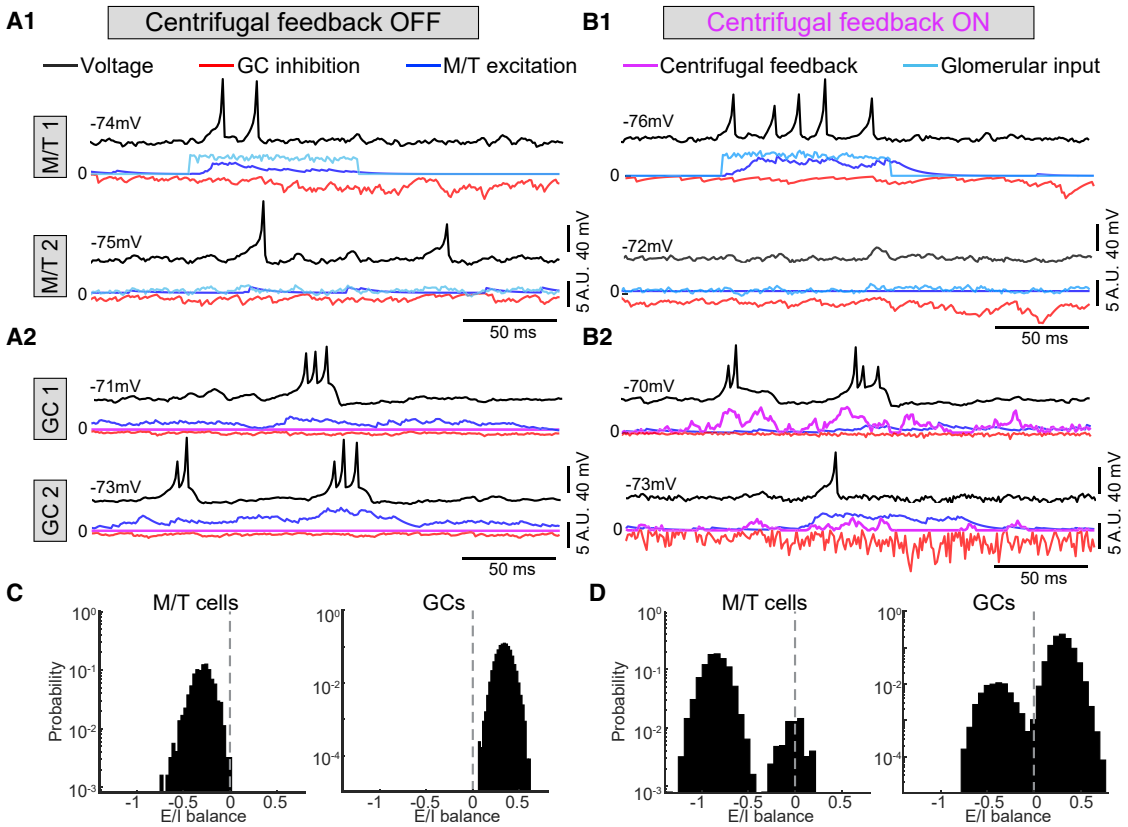

Figure 3. Feedback modulates the interaction between excitatory and inhibitory (E/I) synaptic inputs in MOB cells

(A) Voltage trace (top black) and synaptic inputs (bottom) for two M/T cells and GCs when feedback is OFF.

(A1) M/T 1 receives glomerular input (cyan trace) from an odor-activated glomerulus. M/T 2 is connected to a non-activated glomerulus.

(A2) similar to (A1) but for two GCs when feedback (purple trace) is OFF.

(B) Similar to (A) but for feedback ON.

(B1) The same M/T cells as in (A1), but M/T 1 fires persistently throughout glomerular activation, and M/T 2 remains silenced when feedback is ON.

(B2) The same two GCs as in (A2).

(C) Histogram of excitatory and inhibitory synaptic inputs during a sniff for M/T cells (left) and GCs (right) when feedback is OFF. Glomerular input is not included in excitation for M/T cells. Positive values mean that a cell receives more excitation, and a negative value means that the net synaptic input is inhibition.

(D) Similar to (C) but for feedback ON. Excitatory feedback to GCs is included in excitation for GCs.

animal is presented with two odors of varying similarity and trained to respond to one of these stimuli. The more similar the two odors, the more overlapping their neural representations. A measure of computation would be how network activity renders the patterns of PCx activity for these two representations more distinct.

We first presented two model odors (Figure 1B) to the network and studied the responses of PC cells. When feedback was OFF, both odors evoked a transient burst of spikes followed by a sharp truncation and persistent suppression in the PCx. As a consequence, the PC population firing rates were largely overlapping (Figure 5A). When feedback was ON, however, the PC population firing rates to different odors deviated significantly across time (Figure 5B). To visualize these differences in the activity of large ensembles of PC cells, we performed principal-component analysis (PCA; STAR Methods) and displayed the population dynamics in a low-dimensional space defined by the first three components (Figures 5C and 5D). PC activity to a given odor was a trajectory that began at the origin and extended outward as different glomeruli were activated, returning to baseline at the conclusion of the sniff cycle. Each odor produced a different trajectory. The farther apart the trajectories, the more separable the neural representations of the two odors would be. First, ensemble trajectories for the two odors (Figure 5D) became more separable when feedback was ON compared with when feedback was OFF. This was consistent across a number of odors (Figures 5E and 5F) revealing that the dynamics of PC cells were shaped by the centrifugal inputs to the MOB. Temporal decorrelation in the activity patterns of M/T cells has long been known to be a feature of olfactory coding and odor discrimination (Friedrich, 2001; Gschwend et al., 2015; Kato et al., 2012). Turning feedback ON increased the temporal decorrelation (Figures 5E1 and 5F1), suggesting that one role of feedback may be to enhance the existing mechanisms for odor discrimination by making the population representations of odors more distinct in the PCx (Figure 5E2 and 5F2; Braganza et al., 2020; Chen and Padmanabhan, 2020).

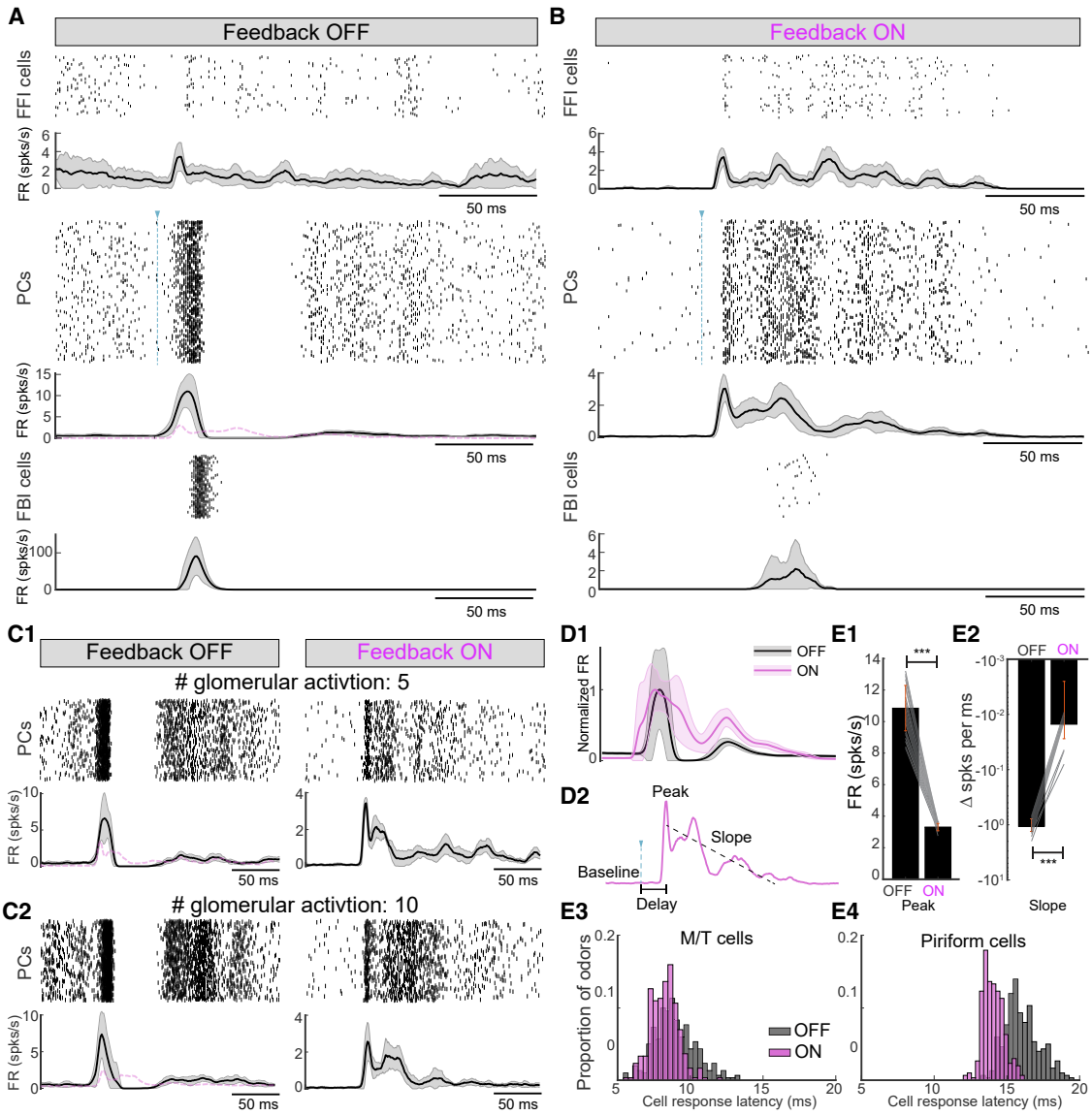

Figure 4. Feedback unravels the temporal structure in firing of piriform cells

(A) Piriform cortical (PC) cell responses to an odor with feedback OFF. Top: spiking activity of individual FFI neurons (raster) and mean firing rate for the population of FFI cells. Center: spiking activity for individual PC cells and mean firing rate for the PC cell population. Bottom: spiking activity for individual FBI neurons and mean firing rate for the population of FBI cells. PC cells fire with a transient burst of spikes that are sharply truncated by local FBIs and followed by persistent suppression. Population firing rates: mean ± SD, $n = 10$ trials. The purple dashed line (center) indicates the average PC cell firing rate for feedback ON. The blue dashed line indicates activation of the earliest glomerulus for the odor.

(B) Similar to (A) but for feedback ON.

(C) Similar to (A) for two odors that activate 5 (C1) or 10 (C2) glomeruli.

(D) Comparison of PC cell population firing rates between feedback OFF and ON.

(D1) PC population firing rate in response to all model odors (mean ± SD, $n = 300$ odors). The traces of feedback OFF and ON are normalized to have the same peak amplitude.

(D2) Schematic to quantify the dynamics of PC population firing rate in response to a single odor. Peak, the first peak in the trial-averaged population firing rate; slope, the slope of a linear function (oblique dashed line) fitted to the mean firing rate between the peak and the first time when it drops below baseline; delay, the latency between the peak and the activation time of the earliest glomerulus defined by the odor (vertical dashed line with a triangle on top).

(E) Comparison of PC dynamics between feedback OFF versus ON.

(E1) Peak firing rate. Connecting lines for 30 example odors are shown (mean ± SD, $n = 300$ odors, *** $p<0.001$, Wilcoxon signed-rank test).

(E2) Similar to E1 but for slope.

(E3) Histogram of the delay across 300 odors. Left: M/T cells. Right: PC cells.

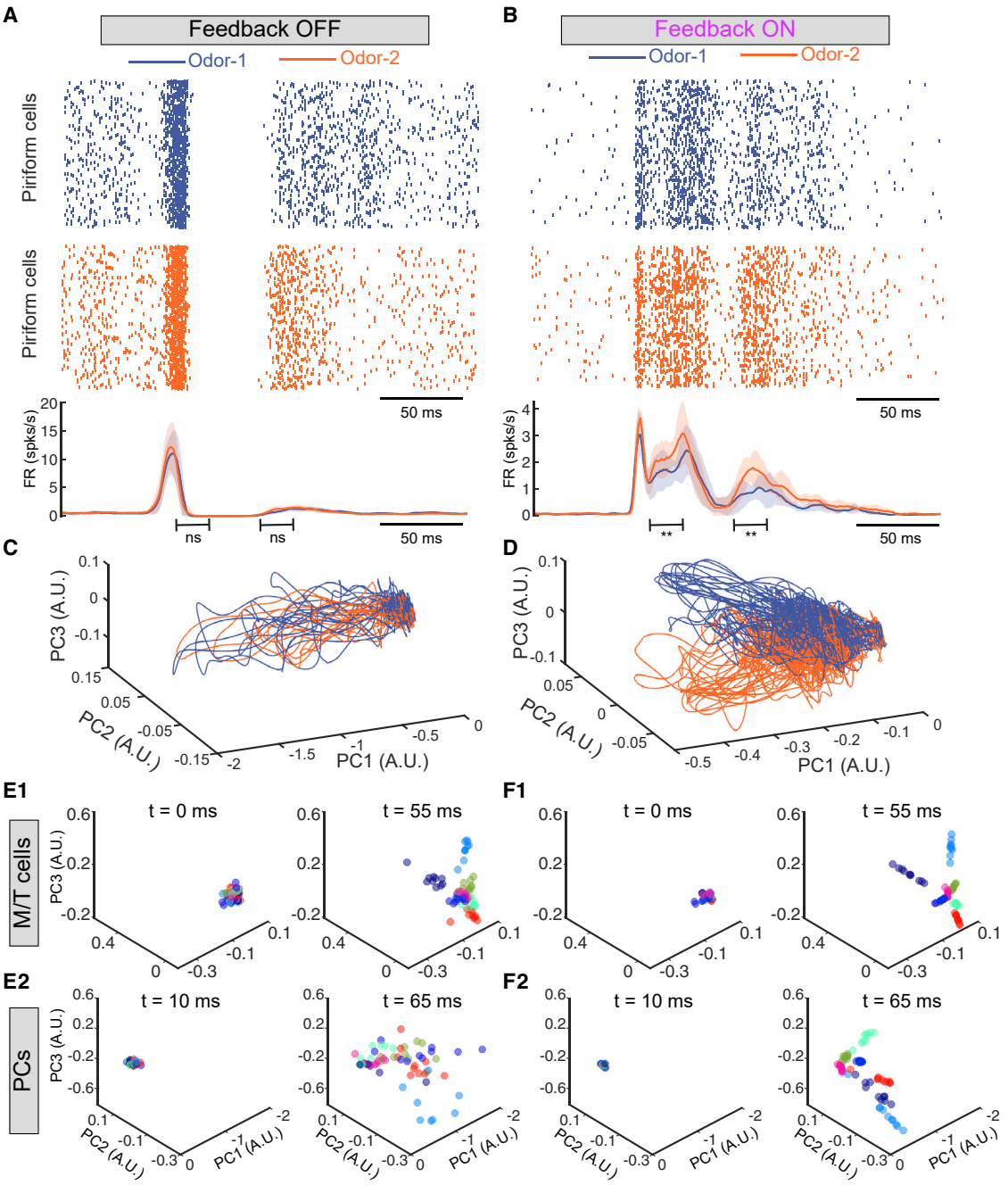

Figure 5. Feedback increases the separation between PC cell responses to different odors

(A) PC cell responses to odor 1 and odor 2 (Figure 1B) with feedback OFF. Top and center: raster plot of PC cell responses to odor 1 and odor 2 in a trial. Bottom: population firing rates of PC cells responding to two odors (mean ± SD, $n = 10$ trials). The firing rate separations between odor 1 and odor 2 are nonsignificant (ns; $p > 0.05$, Wilcoxon rank-sum test).

(B) Similar to (A) but for feedback ON (mean ± SD, $n = 10$ trials). PC cells fire persistently to both odors. The firing rate between odor 1 and odor 2 are significantly different during $70 - 90ms$ and $120 - 140ms$ (**$p < 0.01$, Wilcoxon rank-sum test).

(C) Low-dimensional projections of ensemble trajectories of PC cells onto the first three principal components when feedback is OFF. Each trace corresponds to a single-trial PC cell response to one of the odors (color coded).

(D) Similar to (C) but for feedback ON.

(E) The low-dimensional projected ensemble activity pattern of M/T cells (E1) and PC cells (E2) for feedback OFF. Each dot corresponds to a single-trial ensemble activity, and each color corresponds to a different odor ($n = 7$ odors). The M/T cell ensemble patterns are selected at $t = 0ms$ (left) and $t = 55ms$ (right). The PC cell ensemble patterns are selected at $t = 10ms$ (left) and $t = 65ms$ (right).

(F) Similar to (E) but for feedback ON.

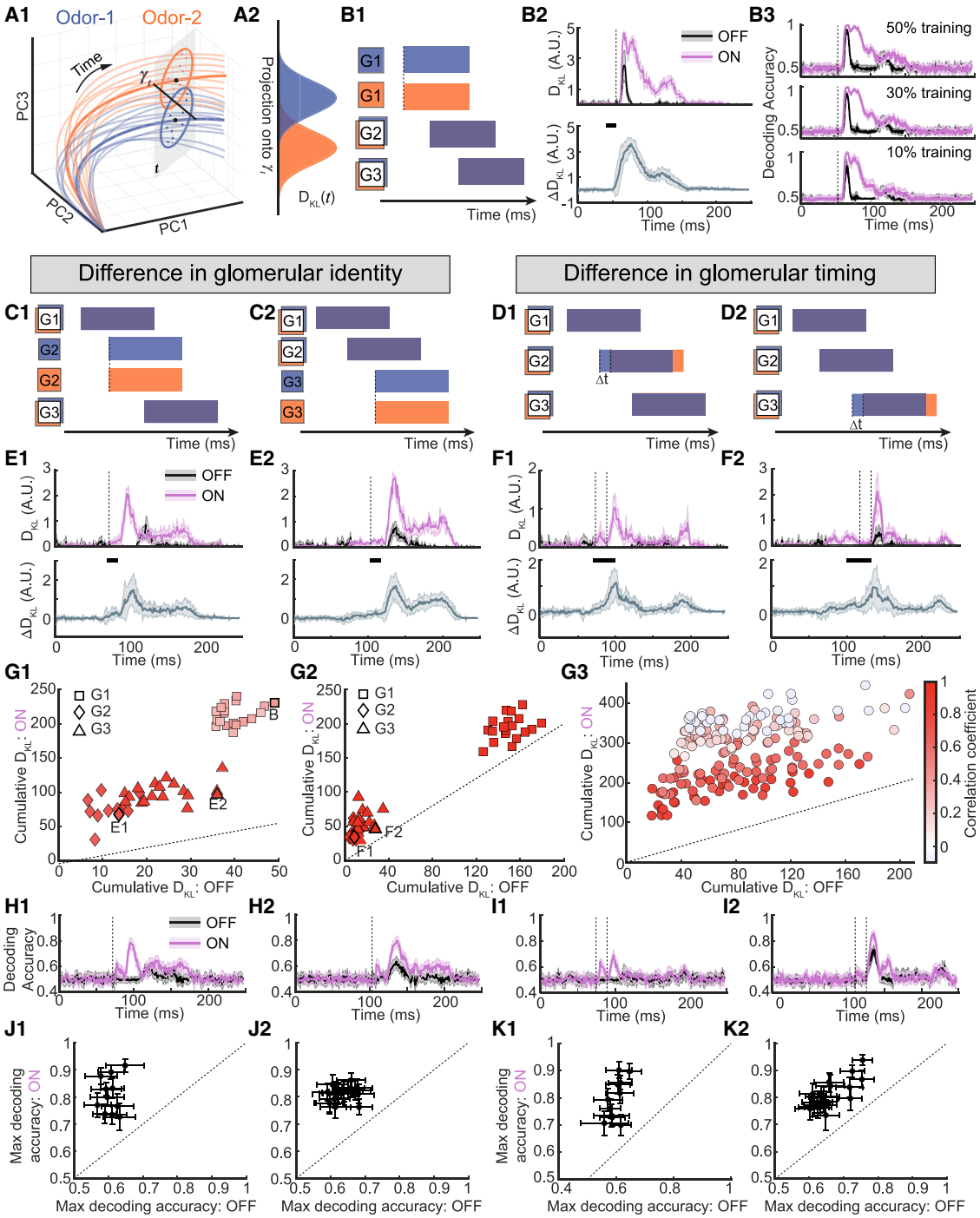

Figure 6. Feedback enhances odor information gain in the PCx

(A) Schematic for quantifying the odor information encoded by PC cell population responses.

(A1) Odor-evoked PC cell responses in low-dimensional space (thick trace, trial-averaged responses; thin trace, single-trial responses). PC cell responses at a single time step t are clusters of points visualized for simplicity on a 2D plane (gray). γ_t is the optimal linear decoder at each time.

(A2) PC responses for two different odors are projected onto γ_t and form two probability distributions.

(B) Symmetrized Kullback-Leibler divergence (D_{KL}) for odor pairs that differ only by the identity of the first glomerulus (G1).

(B1) Schematic of glomerular activation patterns for a pair of model odors (color coded). Glomerular identity is denoted by the vertical position of boxes. G1 boxes are non-overlapping and thus have different identities. G2 boxes (and G3) are overlapping and thus have the same identity. Staggered rectangles indicate glomerular activation.

(legend continued on next page)

Information gain in odor perception achieved by feedback

The previous example highlighted the ways in which changing glomerular identity resulted in differences in encoding in the PCx and would be predicted regardless of whether the system used a combinatorial or temporal code. We next studied how neural representation of an odor in the PCx varied when the identity or timing of later-activated glomeruli was changed. Small changes in concentration or chemical structure could result in changes in the identity or timing of different glomeruli. By defining odors not in terms of their chemical structures but in terms of their glomerular activation patterns, we explored how differences between two odors that activate different glomerular patterns affect coding in the PCx (Carey et al., 2009; Chong et al., 2020; Gire et al., 2013b; Smear et al., 2011; Soucy et al., 2009; Spors and Grinvald, 2002).

First, we systematically varied the identity, timing, or both of activated glomeruli across a total of 192 different model odors. The PC population responses to repeated presentations of one odor were visualized as low-dimensional trajectories (Figure 6A1, thin curves). At any time during a sniff, responses were a cluster of points distributed within the space, reflecting the variability across trials for a given odor (points) and the variability across different odors (color). At each moment in time, we assessed the differences between the two distributions of odors by projecting the points onto a time-varying optimal linear decoder (Figures 6A2 and S6; STAR Methods). The more separable the two distributions were, the more accurately the odor could be decoded from the PC responses and, thus, the more information was encoded in the PCx. We measured the amount of odor information in the PCx by calculating the symmetrized Kullback-Leibler divergence (D_{KL}) (STAR Methods). The more distinct two odor representations, the larger the D_{KL}. For example, at a given time ($t = 31ms$), the PC responses to odor 1 and odor 2 were more easily distinguishable when the feedback switched ON, giving rise to more separable distributions of the PC responses (Figure S6).

We first considered odor pairs that differed only in the identity of a single glomerulus. When the identity of the earliest activated glomerulus (first glomerulus [G1]) was different (Figure 6B1), the D_{KL} increased rapidly regardless of whether feedback was ON or OFF (Figure 6B2, left). In these examples, the information in the spiking activity to the different representations of the two odors was sufficient to distinguish them, independent of whether feedback was ON or OFF. This was consistent with the previous finding that G1 carried the bulk of information about each of the odors (Wesson et al., 2008; Bolding and Franks, 2017; Chong et al., 2020). Interestingly, when feedback was ON, the D_{KL} had a larger magnitude and remained high even after G1 was no longer active (Figure 6B2, right), suggesting that feedback enhanced and maintained odor information gains across the sniff cycle, even after the differences in glomerular activation had already happened. For odor pairs differing in the identity of the second or third activated glomerulus (G2 in Figures 6C1 and 6E1; G3 in Figures 6C2 and 6E2), we observed a significant increase in D_{KL} for feedback ON compared with feedback OFF. These results remained valid even when we used a fixed readout dimension γ obtained from averaging across time and conditions (OFF and ON; Figure S6). As a result, small differences between the two odors being discriminated that would result in small differences in activation of the second or third glomerulus could be informative to the PCx when feedback was ON (Schaefer and Margrie, 2007). If the PCx could represent differences in glomerular identity as differences in the timing of piriform activity patterns, then could feedback also enable the PCx to encode differences in the activation timing of glomeruli? When we presented model odors that activated the same subset of glomeruli but with different onset latencies (Δt = 15 ms), turning feedback ON significantly increased the D_{KL} for odors differing in activation timing of the second or third glomerulus (Figures 6D and 6F).

(B2) Top: D_{KL} for one odor pair when feedback is ON or OFF (mean ± SD, $n = 10$ trials). Bottom: difference of D_{KL} (ΔD_{KL} = ON− OFF) across different odor pairs differing in G1 identity (mean ± SD, $n = 19$ odor pairs).
(B3) Decoding accuracy for the odor pair in (B2), top, using the K nearest neighbor algorithm. Three nearest neighbors are used, and different percentages of data are used for training. Mean ± SD, $n = 30$ trials.
(C) Similar to (B1) but for glomerular identity difference only in G2 (C1) or G3 (C2).
(D) Similar to (C) but for timing differences in G2 (D1) or G3 (D2) by $\Delta t = 15$ ms. In this schematic, the boxes for G1, G2, and G3 are overlapping, but the staggered rectangles are shifted by Δt.
(E) D_{KL} and ΔD_{KL} for glomerular identity difference only in G2 (E1) or G3 (E2). Top: D_{KL} for one odor pair (mean ± SD, $n = 10$ trials). Bottom: ΔD_{KL} across different odor pairs (mean ± SD, $n = 11$ odor pairs for E1, $n = 18$ odor pairs for E2).
(F) Similar to (E) but for glomerular timing difference in G2 (F1) or G3 (F2).
(G) Cumulative D_{KL} over a sniff cycle to quantify the total amount of information in the PCx.
(G1) For odor pairs differing in the identity of a single glomerulus (same data as in B2 and E). Identity difference in G1, G2, or G3 is denoted by different shapes. Dotted line, unity.
(G2) Similar to (G1) but for odor pairs differing in activation timing of a single glomerulus; same data as in (F).
(G3) Similar to (G1) and (G2) but for odor pairs with a combination of identity and timing difference in one or multiple glomeruli. Each circle denotes one odor pair, and the color represents pairwise correlation between two odors and, thus, similarity.
(H) Decoding accuracy for the odor pairs in (E), top, using the K nearest neighbor algorithm. Three nearest neighbors are used, and 30% of data are used for training.
(H1) The odor pair differs in the identity of G2. Error bars: mean ± SD, n = 30 trials.
(H2) The odor pair differs in the identity of G3. Error bars: mean ± SD, $n = 30$ trials.
(I) Similar to (H) but for the odor pairs in (F), top. The odor pair differs in the timing of G2 (I1) and G3 (I2). Mean ± SD, $n = 30$ trials.
(J) Maximum decoding accuracy for multiple odor pairs with glomerular identity difference in G2 (J1, $n = 11$ odor pairs) or G3 (J2, $n = 18$ odor pairs). Three nearest neighbors are used, and 30% of data are used for training. Mean ± SD, $n = 30$ trials.
(K) Similar to (J) but for multiple odor pairs with a glomerular timing difference in G2 (K1) or G3 (K2).

To ensure that our result was not due to features of the D_{KL} analysis, we also implemented a linear decoder analysis using the K nearest neighbor algorithm (STAR Methods). Consistent with our D_{KL} analysis, turning feedback ON increased the accuracy of the linear decoder for identity and timing differences in glomerular activation (Figures 6B3 and 6H–6K). The numbers of nearest neighbors and proportion of training data did not affect the results (Figure S7), demonstrating that feedback increased the odor information and decoding accuracy in the PCx across different metrics of coding efficiency.

We summarized the differences in coding across all odors using the cumulative D_{KL}, which served as a measurement of the total amount of information gained from the differential activation of glomeruli between odor pairs. When feedback was ON, a significant increase occurred in the information in spiking patterns across odors that differed in identity or timing over the three activated glomeruli (Figures 6G1 and 6G2). Activating feedback increased the information gain between two different odors regardless of their similarity, as measured by the input correlation (range, 0.1–0.9; Figure 6G3). Our results revealed a functional role for feedback: effective encoding of glomerular identity and timing using the temporal structure and combinatorial patterns of cell activity in the PCx.

Feedback improves behavioral performance in odor discrimination

Our analysis left open the question of whether this information could be utilized by animals in decision-making. For example, what, if any, effect would controlling feedback have on an animal's behavioral performance when asked to distinguish between two odors? Did the feedback circuit affect the accuracy (how often mistakes are made) or reaction time (how long a response takes) in an odor discrimination task? Such behavioral measurements are performed in animal experiments and can act as a proxy for the information in the PCx to which animals actually have access (Abraham et al., 2010; Uchida and Mainen, 2003).

We bridged the gap between neural coding and behaviors using a two-alternative forced choice (2AFC) task (STAR Methods) and then applying the sequential probability ratio test (SPRT) (Bogacz et al., 2006; Gold and Shadlen, 2007) to model behavioral performance. On each trial, a randomly chosen odor (odor 1 or odor 2) was presented, with the odor onset aligning to the start of a sniff. During a sniff cycle, noisy momentary evidence was gained from observing the PC responses sampled from the odor-evoked probability distribution (Figures 7A1 and 7A2). A choice was made when the accumulated evidence reached one of the decision boundaries (Figure 7A3), and the reaction time was recorded to account the decision and a motor delay (normally distributed with mean $= 50ms$ and SD $= 5ms$). Because only one sniff has been shown to be sufficient for the animal to make decisions (Uchida and Mainen, 2003; Wesson et al., 2008), the model was constructed to report which odor was presented by the end of a single sniff (odor 1 or odor 2). If neither decision boundary was reached before the end of the sniff, the choice was made by chance ($P(Odor-1) = P(Odor-2) = 0.5$), equivalent to a random guess the animal might make because it could not distinguish between the two odors.

To examine how accuracy and reaction time of discrimination were influenced by odor similarity, we varied the glomerular timing between two odors by $5ms$ increments in each glomerulus. The larger the difference in glomerular timing, the more different the two odors were. Such differences corresponded to differences in odor concentration or odor identity (Meister and Bonhoeffer, 2001; Schaefer and Margrie, 2007) in a discrimination task requiring the animal to discriminate between two similar odors or between different concentrations of a single odor. The differences the animal perceives would be due to differences in the timing of the activated glomeruli. First, when we simulated differences in timing of G1 between the two odors (Figure 7B1), the accuracy increased and the reaction time was reduced, regardless of whether feedback was OFF or ON (Figure 7C1), a result consistent with previous studies (Palmer et al., 2005; Uchida and Mainen, 2003). However, for any given difference in glomerular timing associated with two different odors, switching feedback ON increased the accuracy and reduced the reaction time, corresponding to an improvement in the animal's behavioral performance. For subsequent glomeruli, differences in the timing of glomerular activity could occur bidirectionally; i.e., glomerulus 2 (G2) activated by odor 1 could occur earlier (negative values) or later (positive values) than G2 for odor 2 (Figures 7B2 and 7B3). For both timing shifts associated with G2 or G3, the discrimination performance was improved when the feedback was ON (Figures 7C2 and 7C3). Interestingly, shifting the G2 or G3 latencies earlier resulted in larger changes in accuracy and reaction time compared with shifting them later, providing further support for the importance of the earliest activated glomeruli in guiding odor discrimination behaviors (Chong et al., 2020; Wilson et al., 2017). A temporal shift of $-45ms$ in G2 latency for one odor would mean that G2 becomes the first one activated, making it G1. The resultant alternation in the order of glomerular activation would render the differences between the two odors differences in glomerular identity rather than timing. As a consequence, we observed a steep rise in accuracy (a more than 10% increase from $-40ms$ to $-45ms$) as well as a decline in the reaction time (a more than $50ms$ reduction from $-40ms$ to $-45ms$), echoing the important role of the earliest activated glomerulus in odor perception. Our results revealed the essential role of feedback in shaping how odor information could guide animal behavior in this example of an odor discrimination task.

DISCUSSION

Using a spiking neuronal network model that recapitulated the details of circuit architecture within and between the MOB and PCx, we identified a role of feedback. The PCx was able to extract information about odors from the identity and timing of activation patterns across M/T cells. When the feedback was OFF, PC cells responded transiently to the earliest activated glomerulus, consistent with the models of olfactory coding, where the combinatorial pattern of activated cells is used to represent odors (Stern et al., 2018). When the feedback weights to the local inhibitory interneurons (GCs) in the MOB were ON, PC cells fired persistently throughout odor presentation. The temporal structure of PC cells reflected the successive activation of the M/T cell population by different glomeruli and was

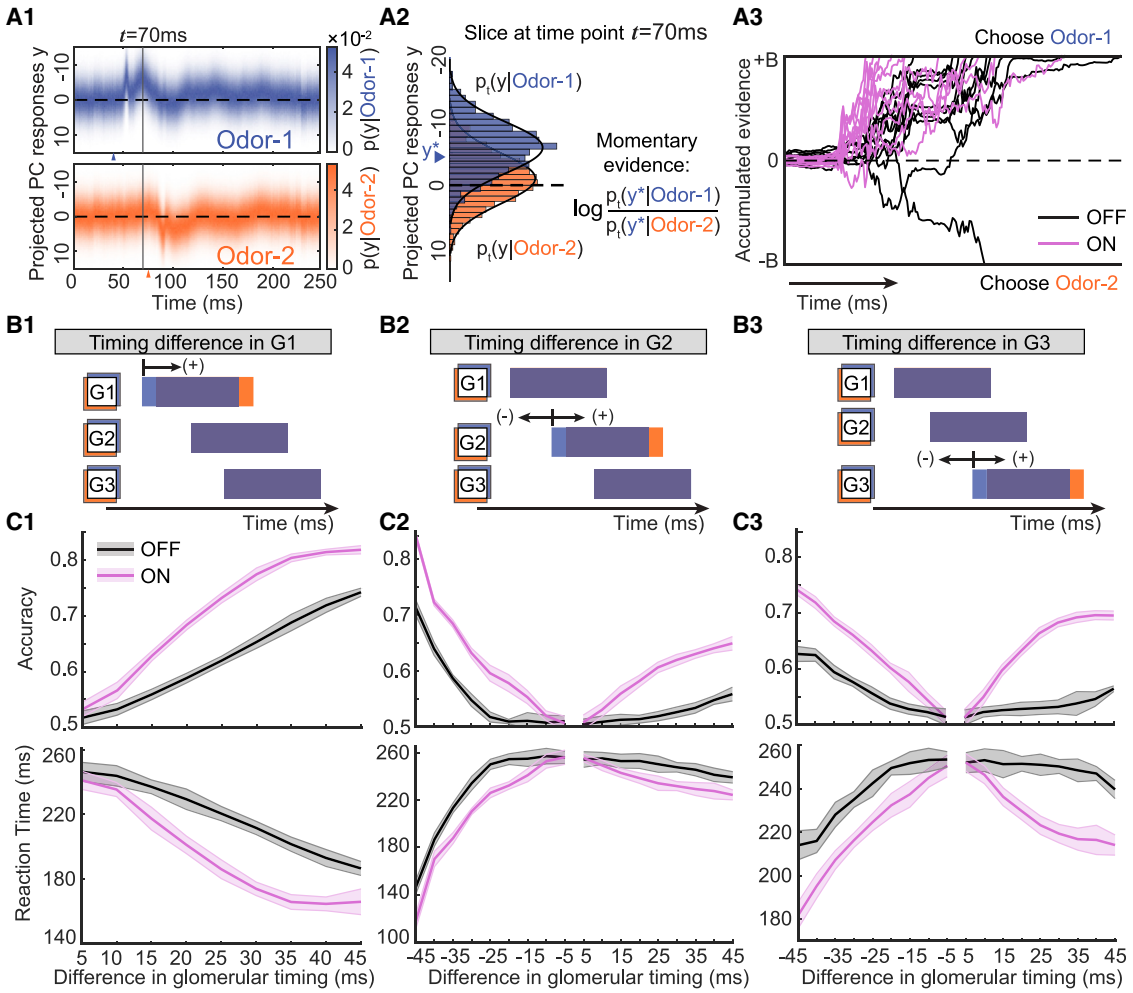

Figure 7. Feedback improves behavioral performance in odor discrimination

(A) Decision-making modeled as an evidence accumulation process according to sequential probability ratio test (SPRT).

(A1) The time-varying probability distribution of the projected PC cell responses along γ_t to two odors differing only in activation timing of G1 by 35*ms*. The triangles at the bottom indicate the activation timing of the earliest glomerulus (G1). The gray vertical lines indicate the slice at $t = 70ms$.

(A2) The distributions sliced at $t = 70ms$ in (A1). A sample y^* is generated by the distribution of odor 1 (assuming odor 1 is presented). The momentary evidence at this time step is calculated by the log likelihood ratio of the sample.

(A3) Traces of the accumulated evidence over time for feedback ON or OFF. A decision is made when the boundary $\pm B$ is reached. Otherwise, a choice is made by chance at the end of the sniff.

(B) Schematic of temporally shifting the activation timing of each glomerulus.

(B1) Temporal shift in G1.

(B2) Bidirectional temporal shift in G2.

(B3) Bidirectional temporal shift in G3.

(C) The accuracy and reaction time as a function of the timing differences in glomerular activation (mean ± SD, $n = 10$ agents).

(C1) Timing differences in G1 activation (odor 1: G1, 40*ms*; G2, 86*ms*; G3, 177*ms*; odor-2: G1, $40ms + \Delta t$; G2/G3: the same as odor 1).

(C2) Timing differences in G2 activation (odor 1: G1, 40*ms*; G2, 78*ms*; G3, 113*ms*; odor 2: G2, $78ms \pm \Delta t$; G1/G3: the same as odor 1).

(C3) Timing differences in G3 activation (odor 1: G1, 54*ms*; G2, 81*ms*; G3, 120*ms*; odor-2: G3, $120ms \pm \Delta t$; G1/G2: the same as odor 1).

informative about odors. Activity patterns across the PC population to different odors were consequently more separable with feedback ON. This effect was robust to differences in identity or timing of the earliest or later-activated glomeruli over the course of a sniff. In an odor discrimination task, increased information in PCx activity patterns resulted in improved behavioral performance regarding accuracy and reaction time. Our findings align with experimental results summarized in Table S4.

Many coding strategies have been proposed based on the structure of neural circuits and the activity patterns in the early olfactory system. Features of odors, including their identity and concentration, are represented in the temporal patterns of glomerular activation (Baker et al., 2019; Rubin and Katz, 1999; Spors and Grinvald, 2002; Vincis et al., 2012) and result in differences in the identity and timing of activated M/T cells (Bathellier et al., 2008; Cury and Uchida, 2010; Kay and Laurent, 1999). In

the PCx, this temporal information from the bulb is remapped onto a combinatorial pattern of activity across piriform cells (Bolding and Franks, 2017; Stern et al., 2018; Stettler and Axel, 2009). Such a coding strategy is attractive for a number of reasons. First, the random connectivity of M/T cells to individual PC neurons provides an anatomical underpinning for a combinatorial code (Sosulski et al., 2011). Second, such an architecture may be one biological implementation of compressed sensing (Babadi and Sompolinsky, 2014; Ganguli and Sompolinsky, 2012; Stevens, 2015). Finally, neurophysiological studies show that local inhibition within the cortex (Bekkers and Suzuki, 2013) truncates the activity of PC neurons, restricting patterns of neuronal firing to narrow windows of opportunity (Bolding and Franks, 2017; Miura et al., 2012), analogous to network packets in digital communication.

However, results from recent studies suggest that refinement of this model may be appropriate. First, laboratory studies often control the odor onset and offset experimentally, but natural odor plumes fluctuate across multiple spatial and temporal scales (Ackels et al., 2021; Lewis et al., 2021; Celani et al., 2014; Moore and Atema, 1991; Riffell et al., 2014; Schmuker et al., 2016; Szyszka et al., 2014), making a single window corresponding to odor onset and offset difficult to define. Second, a number of studies have shown that animals use information in the timing of glomerular activation to guide behavior (Chong et al., 2020; Rebello et al., 2014; Smear et al., 2011). Rodents can be trained to discriminate between highly similar odors, and their accuracy is strongly correlated with reaction time (Rinberg et al., 2006; Uchida and Mainen, 2003). Accuracy increases significantly when the mice sample the odor stimulus for longer periods of time (Ackels et al., 2021), suggesting that information is gained throughout odor presentation rather than only at the onset of an odor or within a narrow sniff-locked time window. To maintain the same level of accuracy, mice require more time to discriminate odor pairs with highly overlapping spatial temporal patterns of glomerular activation than odor pairs with dissimilar glomerular patterns (Abraham et al., 2004), suggesting that temporal integration is needed for the olfactory system to discriminate highly similar odors. These data point to a framework in which temporally rich neural codes in the bulb are relayed into the PCx, encoding information about odors in a continuous way. We found that this information is gated by a single flexible circuit, where feedback from the PCx to the bulb determines which critical features of activity are relayed to the olfactory cortex.

If two odors are markedly different, a combinatorial code in the PCx would be sufficient for olfactory discrimination. However, in cases where an odor discrimination task is complex because the two odors activate highly overlapping populations of glomeruli, a change in the top-down weight of feedback would provide access to temporal information in the olfactory code (Chen and Padmanabhan, 2020; Hiratani and Latham, 2020; Schaefer and Margrie, 2007). First, feedback would enhance the signal-to-noise ratio of MOB output. Second, by encoding later-activated glomeruli in the firing of PC cells, feedback would allow time to be an additional dimension with which an animal can gain information about odors. Such a strategy would support encoding of fast fluctuations that occur in odor plumes. The computational benefits of feedback in our model also capture the sparsity of FBI recruitment in the PCx. When FBIs in the olfactory cortex are sparsely recruited under the feedback ON condition, PC cells fire persistently, preserving their temporal coding. Consistent with this idea, performance in odor discrimination degrades quickly as local inhibition in the PCx becomes stronger (Hiratani and Latham, 2020).

We remain agnostic about the mechanisms that flexibly turn centrifugal feedback ON and OFF. Changes in top-down control may correspond to an array of behavioral state changes, including anesthesia (Kato et al., 2012; Rinberg et al., 2006). State differences would affect not only feedback from the PCx but also other signals, including neuromodulators (Brill et al., 2016). Neuromodulators such as serotonin act on short axon cells (via 5HT 2C receptors) (Brill et al., 2016; Petzold et al., 2009) and M/T cells (Kapoor et al., 2016). Differences in performance observed across trials in animal studies (Chong et al., 2020; Gill et al., 2020) may thus reflect differences in neuromodulatory state across those trials. Feedback weights could also change because of synaptic plasticity. Several studies have shown that the PCx is involved in olfactory learning (Cohen et al., 2008; Hasselmo and Bower, 1990; Litaudon et al., 1997), and long-term potentiation (LTP) and plasticity in the PCx can regulate activity in the bulb (Cauthron and Stripling, 2014). Here, switching between feedback ON and OFF would be akin to changing synaptic weights over the course of learning. Finally, changes in the weights of feedback may be due to adult neurogenesis (Lledo et al., 2005; Arenkiel et al., 2011; Deshpande et al., 2013). The integration and response properties of these adult-born GCs are dependent on sensory experience (Alonso et al., 2006; Lepousez et al., 2014; Livneh et al., 2009; Rochefort et al., 2002), which may require piriform feedback (Wu et al., 2020). As a consequence, the structure of connections from the PCx to GCs are likely not random but contain information about olfactory learning (Livneh and Mizrahi, 2012; Sailor et al., 2016).

Limitations of the study

First, our computational model isolates top-down feedback from the PCx, but there are multiple sources of feedback to the bulb (Padmanabhan et al., 2019). Second, our model does not consider the influence of neuromodulators that affect network dynamics throughout the early olfactory system. Despite these limitations, our results identify a framework for how feedback could influence animal behavior on diverse time scales.

The PCx affects the temporal structure of activity patterns it receives. This modulation likely depends on how different behaviors in the lab or in the wild engage feedback circuits (Ackels et al., 2021; Bolding and Franks, 2018; Boyd et al., 2012; Chong et al., 2020; Gill et al., 2020; Otazu et al., 2015; Wu et al., 2020). We propose that these differences in the temporal activity patterns of the PCx reveal a mode for sensory processing, where information about odor identity and concentration is flexibly shifted, depending on the different ethological demands that are placed on the animal.

STAR★METHODS

Detailed methods are provided in the online version of this paper and include the following:

SUPPLEMENTAL INFORMATION

Supplemental information can be found online at https://doi.org/10.1016/j.celrep.2022.110545.

ACKNOWLEDGMENTS

This study was supported by National Institutes of Health (NIH) R01 MH113924, National Science Foundation (NSF) CAREER 1749772, the Cystinosis Research Foundation, and the Kilian J. and Caroline F. Schmitt Foundation. We thank Doug Portman, Julian Meeks, and three anonymous reviewers for their feedback.

AUTHOR CONTRIBUTIONS

K.P. conceived and supervised the project. Z.C. performed the experiments and analyses. Z.C. and K.P. created the figures and wrote the manuscript. Both authors approved the submitted version.

DECLARATION OF INTERESTS

The authors declare no competing interests.

Received: August 12, 2021
Revised: December 30, 2021
Accepted: March 1, 2022
Published: March 22, 2022

REFERENCES

Abraham, N., Spors, H., Carleton, A., Margrie, T., Kuner, T., and Schaefer, A. (2004). Maintaining accuracy at the expense of speedstimulus similarity defines odor discrimination time in mice. Neuron *44*, 865–876.

Abraham, N.M., Egger, V., Shimshek, D.R., Renden, R., Fukunaga, I., Sprengel, R., Seeburg, P.H., Klugmann, M., Margrie, T.W., Schaefer, A.T., et al. (2010). Synaptic inhibition in the olfactory bulb accelerates odor discrimination in mice. Neuron *65*, 399–411.

Ackels, T., Erskine, A., Dasgupta, D., Marin, A.C., Warner, T.P.A., Tootoonian, S., Fukunaga, I., Harris, J.J., and Schaefer, A.T. (2021). Fast odour dynamics are encoded in the olfactory system and guide behaviour. Nature *593*, 558–563.

Babadi, B., and Sompolinsky, H. (2014). Sparseness and expansion in sensory representations. Neuron *83*, 1213–1226.

Baker, K.L., Vasan, G., Gumaste, A., Pieribone, V.A., and Verhagen, J.V. (2019). Spatiotemporal dynamics of odor responses in the lateral and dorsal olfactory bulb. PLoS Biol. *17*, e3000409.

Bathellier, B., Buhl, D.L., Accolla, R., and Carleton, A. (2008). Dynamic ensemble odor coding in the mammalian olfactory bulb: sensory information at different timescales. Neuron *57*, 586–598.

Bekkers, J.M., and Suzuki, N. (2013). Neurons and circuits for odor processing in the piriform cortex. Trends Neurosciences *36*, 429–438.

Bogacz, R., Brown, E., Moehlis, J., Holmes, P., and Cohen, J.D. (2006). The physics of optimal decision making: a formal analysis of models of performance in two-alternative forced-choice tasks. Psychol. Rev. *113*, 700–765.

Bolding, K.A., and Franks, K.M. (2017). Complementary codes for odor identity and intensity in olfactory cortex. ELife *6*, e22630.

Bolding, K.A., and Franks, K.M. (2018). Recurrent cortical circuits implement concentration-invariant odor coding. Science *14*, eaat6904.

Boyd, A.M., Sturgill, J.F., Poo, C., and Isaacson, J.S. (2012). Cortical feedback control of olfactory bulb circuits. Neuron *76*, 1161–1174.

Braganza, O., Müller-Komorowska, D., Kelly, T., and Beck, H. (2020). Quantitative properties of a feedback circuit predict frequency-dependent pattern separation. Elife *9*, e53148.

Buck, L., and Axel, R. (1991). A novel multigene family may encode odorant receptors: a molecular basis for odor recognition. Cell *65*, 175–187.

Burton, S.D., and Urban, N.N. (2015). Rapid feedforward inhibition and asynchronous excitation regulate granule cell activity in the mammalian main olfactory bulb. J. Neurosci. *35*, 14103–14122.

Carey, R.M., Verhagen, J.V., Wesson, D.W., Pírez, N., and Wachowiak, M. (2009). Temporal structure of receptor neuron input to the olfactory bulb imaged in behaving rats. J. Neurophysiol. *101*, 1073–1088.

Celani, A., Villermaux, E., and Vergassola, M. (2014). Odor landscapes in turbulent environments. Phys. Rev. X *4*, 041015.

Chen, Z., and Padmanabhan, K. (2020). Top-down control of inhibitory granule cells in the main olfactory bulb reshapes neural dynamics giving rise to a diversity of computations. Front. Comput. Neurosci. *14*, 59.

Chockanathan, U., Crosier, E.J., Waddle, S., Lyman, E., Gerkin, R.C., and Padmanabhan, K. (2021). Changes in pairwise correlations during running reshape global network state in the main olfactory bulb. J. Neurophysiol. *125*, 1612–1623.

Choi, G.B., Stettler, D.D., Kallman, B.R., Bhaskar, S.T., Fleischmann, A., and Axel, R. (2011). Driving opposing behaviors with ensembles of piriform neurons. Cell *146*, 1004–1015.

Chong, E., and Rinberg, D. (2018). Behavioral readout of spatio-temporal codes in olfaction. Curr. Opin. Neurobiol. *52*, 18–24.

Chong, E., Moroni, M., Wilson, C., Shoham, S., Panzeri, S., and Rinberg, D. (2020). Manipulating synthetic optogenetic odors reveals the coding logic of olfactory perception. Science *368*, eaba2357.

Connors, B.W., and Gutnick, M.J. (1990). Intrinsic firing patterns of diverse neocortical neurons. Trends Neurosciences *13*, 99–104.

Cury, K.M., and Uchida, N. (2010). Robust odor coding via inhalation-coupled transient activity in the mammalian olfactory bulb. Neuron *68*, 570–585.

Davison, I.G., and Ehlers, M.D. (2011). Neural circuit mechanisms for pattern detection and feature combination in olfactory cortex. Neuron *70*, 82–94.

Dhawale, A.K., Hagiwara, A., Bhalla, U.S., Murthy, V.N., and Albeanu, D.F. (2010). Non-redundant odor coding by sister mitral cells revealed by light addressable glomeruli in the mouse. Nat. Neurosci. *13*, 1404–1412.

Egger, V. (2005). Dendrodendritic synaptic signals in olfactory bulb granule cells: local spine boost and global low-threshold spike. J. Neurosci. *25*, 3521–3530.

Fantana, A.L., Soucy, E.R., and Meister, M. (2008). Rat olfactory bulb mitral cells receive sparse glomerular inputs. Neuron *59*, 802–814.

Friedrich, R.W. (2001). Dynamic optimization of odor representations by slow temporal patterning of mitral cell activity. Science *291*, 889–894.

Ganguli, S., and Sompolinsky, H. (2012). Compressed sensing, sparsity, and dimensionality in neuronal information processing and data analysis. Annu. Rev. Neurosci. *35*, 485–508.

Ghosh, S., Larson, S.D., Hefzi, H., Marnoy, Z., Cutforth, T., Dokka, K., and Baldwin, K.K. (2011). Sensory maps in the olfactory cortex defined by long-range viral tracing of single neurons. Nature *472*, 217–220.

Gibson, J.R., Beierlein, M., and Connors, B.W. (1999). Two networks of electrically coupled inhibitory neurons in neocortex. Nature *402*, 75–79.

Gill, J.V., Lerman, G.M., Zhao, H., Stetler, B.J., Rinberg, D., and Shoham, S. (2020). Precise Holographic manipulation of olfactory circuits reveals coding features determining perceptual detection. Neuron *108*, 382–393.e5.

Gire, D.H., Restrepo, D., Sejnowski, T.J., Greer, C., De Carlos, J.A., and Lopez-Mascaraque, L. (2013a). Temporal processing in the olfactory system: can we see a smell? Neuron *78*, 416–432.

Gire, D.H., Whitesell, J.D., Doucette, W., and Restrepo, D. (2013b). Information for decision-making and stimulus identification is multiplexed in sensory cortex. Nat. Neurosci. *16*, 991–993.

Gold, J.I., and Shadlen, M.N. (2007). The neural basis of decision making. Annu. Rev. Neurosci. *30*, 535–574.

Gottfried, J.A. (2010). Central mechanisms of odour object perception. Nat. Rev. Neurosci. *11*, 628–641.

Gschwend, O., Abraham, N.M., Lagier, S., Begnaud, F., Rodriguez, I., and Carleton, A. (2015). Neuronal pattern separation in the olfactory bulb improves odor discrimination learning. Nat. Neurosci. *18*, 1474–1482.

Gschwend, O., Beroud, J., Vincis, R., Rodriguez, I., and Carleton, A. (2016). Dense encoding of natural odorants by ensembles of sparsely activated neurons in the olfactory bulb. Sci. Rep. *6*, 36514.

Haddad, R., Lanjuin, A., Madisen, L., Zeng, H., Murthy, V.N., and Uchida, N. (2013). Olfactory cortical neurons read out a relative time code in the olfactory bulb. Nat. Neurosci. *16*, 949–957.

Hiratani, N., and Latham, P.E. (2020). Rapid Bayesian learning in the mammalian olfactory system. Nat. Commun. *11*, 3845.

Johnson, B.A., and Leon, M. (2007). Chemotopic odorant coding in a mammalian olfactory system. J. Comp. Neurol. *503*, 1–34.

Kapoor, V., and Urban, N.N. (2006). Glomerulus-specific, long-latency activity in the olfactory bulb granule cell network. J. Neurosci. *26*, 11709–11719.

Kato, H.K., Chu, M.W., Isaacson, J.S., and Komiyama, T. (2012). Dynamic sensory representations in the olfactory bulb: modulation by wakefulness and experience. Neuron *76*, 962–975.

Kay, L.M., and Laurent, G. (1999). Odor- and context-dependent modulation of mitral cell activity in behaving rats. Nat. Neurosci. *2*, 1003–1009.

Koulakov, A.A., and Rinberg, D. (2011). Sparse incomplete representations: a potential role of olfactory granule cells. Neuron *72*, 124–136.

Laurent, G. (2002). Olfactory network dynamics and the coding of multidimensional signals. Nat. Rev. Neurosci. *3*, 884–895.

Lewis, S.M., Xu, L., Rigolli, N., Tariq, M.F., Suarez, L.M., Stern, M., Seminara, A., and Gire, D.H. (2021). Plume dynamics structure the spatiotemporal activity of mitral/tufted cell networks in the mouse olfactory bulb. Front. Cell. Neurosci. *15*, 633757.

Livneh, Y., and Mizrahi, A. (2012). Experience-dependent plasticity of mature adult-born neurons. Nat. Neurosci. *15*, 26–28.

Lledo, P.-M., Gheusi, G., and Vincent, J.-D. (2005). Information processing in the mammalian olfactory system. Physiol. Rev. *85*, 281–317.

Malnic, B., Hirono, J., Sato, T., and Buck, L.B. (1999). Combinatorial receptor codes for odors. Cell *96*, 713–723.

Markopoulos, F., Rokni, D., Gire, D.H., and Murthy, V.N. (2012). Functional properties of cortical feedback projections to the olfactory bulb. Neuron *76*, 1175–1188.

Meister, M., and Bonhoeffer, T. (2001). Tuning and topography in an odor map on the rat olfactory bulb. J. Neurosci. *21*, 1351–1360.

Miura, K., Mainen, Z.F., and Uchida, N. (2012). Odor representations in olfactory cortex: distributed rate coding and decorrelated population activity. Neuron *74*, 1087–1098.

Miyamichi, K., Amat, F., Moussavi, F., Wang, C., Wickersham, I., Wall, N.R., Taniguchi, H., Tasic, B., Huang, Z.J., He, Z., et al. (2011). Cortical representations of olfactory input by trans-synaptic tracing. Nature *472*, 191–196.

Mombaerts, P., Wang, F., Dulac, C., Chao, S.K., Nemes, A., Mendelsohn, M., Edmondson, J., and Axel, R. (1996). Visualizing an olfactory sensory map. Cell *87*, 675–686.

Moore, P.A., and Atema, J. (1991). Spatial information in the three-dimensional fine structure of an aquatic odor plume. Biol. Bull. *181*, 408–418.

Nelson, S.B., and Valakh, V. (2015). Excitatory/inhibitory balance and circuit homeostasis in autism spectrum disorders. Neuron *87*, 684–698.

Oswald, A.-M., and Urban, N.N. (2012). There and back again: the corticobulbar loop. Neuron *76*, 1045–1047.

Otazu, G.H., Chae, H., Davis, M.B., and Albeanu, D.F. (2015). Cortical feedback decorrelates olfactory bulb output in awake mice. Neuron *86*, 1461–1477.

Ozeki, H., Finn, I.M., Schaffer, E.S., Miller, K.D., and Ferster, D. (2009). Inhibitory stabilization of the cortical network underlies visual surround suppression. Neuron *62*, 578–592.

Padmanabhan, K., and Urban, N.N. (2010). Intrinsic biophysical diversity decorrelates neuronal firing while increasing information content. Nat. Neurosci. *13*, 1276–1282.

Padmanabhan, K., and Urban, N.N. (2014). Disrupting information coding via block of 4-AP-sensitive potassium channels. J. Neurophysiol. *112*, 1054–1066.

Padmanabhan, K., Osakada, F., Tarabrina, A., Kizer, E., Callaway, E.M., Gage, F.H., and Sejnowski, T.J. (2016). Diverse representations of olfactory information in centrifugal feedback projections. J. Neurosci. *36*, 7535–7545.

Padmanabhan, K., Osakada, F., Tarabrina, A., Kizer, E., Callaway, E.M., Gage, F.H., and Sejnowski, T.J. (2019). Centrifugal inputs to the main olfactory bulb revealed through whole brain circuit-mapping. Front. Neuroanat. *12*, 115.

Palmer, J., Huk, A.C., and Shadlen, M.N. (2005). The effect of stimulus strength on the speed and accuracy of a perceptual decision. J. Vis. *30*, 376–404.

Paoli, M., Albi, A., Zanon, M., Zanini, D., Antolini, R., and Haase, A. (2018). Neuronal response latencies encode first odor identity information across subjects. J. Neurosci. *38*, 9240–9251.

Price, J.L., and Powell, T.P.S. (1970). An experimental study of the origin and the course of the centrifugal fibres to the olfactory bulb in the rat. *23*, 215–237.

Rebello, M.R., McTavish, T.S., Willhite, D.C., Short, S.M., Shepherd, G.M., and Verhagen, J.V. (2014). Perception of odors linked to precise timing in the olfactory system. PLoS Biol. *12*, e1002021.

Riffell, J.A., Shlizerman, E., Sanders, E., Abrell, L., Medina, B., Hinterwirth, A.J., and Kutz, J.N. (2014). Flower discrimination by pollinators in a dynamic chemical environment. Science *344*, 1515–1518.

Rinberg, D., Koulakov, A., and Gelperin, A. (2006). Speed-accuracy tradeoff in olfaction. Neuron *51*, 351–358.

Rubin, B.D., and Katz, L.C. (1999). Optical imaging of odorant representations in the mammalian olfactory bulb. Neuron *23*, 499–511.

Sailor, K.A., Valley, M.T., Wiechert, M.T., Riecke, H., Sun, G.J., Adams, W., Dennis, J.C., Sharafi, S., Ming, G., Song, H., et al. (2016). Persistent structural plasticity optimizes sensory information processing in the olfactory bulb. Neuron *91*, 384–396.

Schaefer, A.T., and Margrie, T.W. (2007). Spatiotemporal representations in the olfactory system. Trends Neurosciences *30*, 92–100.

Schmuker, M., Bahr, V., and Huerta, R. (2016). Exploiting plume structure to decode gas source distance using metal-oxide gas sensors. Sensors Actuators B Chem. *235*, 636–646.

Shipley, M.T., and Adamek, G.D. (1984). The connections of the mouse olfactory bulb: a study using orthograde and retrograde transport of wheat germ agglutinin conjugated to horseradish peroxidase. Brain Res. Bull. *12*, 669–688.

Shusterman, R., Smear, M.C., Koulakov, A.A., and Rinberg, D. (2011). Precise olfactory responses tile the sniff cycle. Nat. Neurosci. *14*, 1039–1044.

Smear, M., Shusterman, R., O'Connor, R., Bozza, T., and Rinberg, D. (2011). Perception of sniff phase in mouse olfaction. Nature *479*, 397–400.

Sosulski, D.L., Bloom, M.L., Cutforth, T., Axel, R., and Datta, S.R. (2011). Distinct representations of olfactory information in different cortical centres. Nature *472*, 213–216.

Soucy, E.R., Albeanu, D.F., Fantana, A.L., Murthy, V.N., and Meister, M. (2009). Precision and diversity in an odor map on the olfactory bulb. Nat. Neurosci. *12*, 210–220.

Spors, H., and Grinvald, A. (2002). Spatio-temporal dynamics of odor representations in the mammalian olfactory bulb. Neuron *34*, 301–315.

Stern, M., Bolding, K.A., Abbott, L., and Franks, K.M. (2018). A transformation from temporal to ensemble coding in a model of piriform cortex. ELife *7*, e34831.

Stettler, D.D., and Axel, R. (2009). Representations of odor in the piriform cortex. Neuron *63*, 854–864.

Stevens, C.F. (2015). What the fly's nose tells the fly's brain. Proc. Natl. Acad. Sci. U S A *112*, 9460–9465.

Suzuki, N., and Bekkers, J.M. (2012). Microcircuits mediating feedforward and feedback synaptic inhibition in the piriform cortex. J. Neurosci. *32*, 919–931.

Szyszka, P., Gerkin, R.C., Galizia, C.G., and Smith, B.H. (2014). High-speed odor transduction and pulse tracking by insect olfactory receptor neurons. Proc. Natl. Acad. Sci. U S A *111*, 16925–16930.

Uchida, N., and Mainen, Z.F. (2003). Speed and accuracy of olfactory discrimination in the rat. Nat. Neurosci. *6*, 1224–1229.

Uchida, N., Poo, C., and Haddad, R. (2014). Coding and transformations in the olfactory system. Annu. Rev. Neurosci. *37*, 363–385.

Urban, N.N., and Sakmann, B. (2002). Reciprocal intraglomerular excitation and intra- and interglomerular lateral inhibition between mouse olfactory bulb mitral cells. J. Physiol. *542*, 355–367.

Vincis, R., Gschwend, O., Bhaukaurally, K., Beroud, J., and Carleton, A. (2012). Dense representation of natural odorants in the mouse olfactory bulb. Nat. Neurosci. *15*, 537–539.

Wachowiak, M., and Cohen, L.B. (2001). Representation of odorants by receptor neuron input to the mouse olfactory bulb. Neuron *32*, 723–735.

Wachowiak, M., Denk, W., and Friedrich, R.W. (2004). Functional organization of sensory input to the olfactory bulb glomerulus analyzed by two-photon calcium imaging. Proc. Natl. Acad. Sci. U S A *101*, 9097–9102.

Wanner, A.A., and Friedrich, R.W. (2020). Whitening of odor representations by the wiring diagram of the olfactory bulb. Nat. Neurosci. *23*, 433–442.

Wesson, D.W., Carey, R.M., Verhagen, J.V., and Wachowiak, M. (2008). Rapid encoding and perception of novel odors in the rat. PLoS Biol. *6*, e82.

Willhite, D.C., Nguyen, K.T., Masurkar, A.V., Greer, C.A., Shepherd, G.M., and Chen, W.R. (2006). Viral tracing identifies distributed columnar organization in the olfactory bulb. Proc. Natl. Acad. Sci. U S A *103*, 12592–12597.

Wilson, C.D., Serrano, G.O., Koulakov, A.A., and Rinberg, D. (2017). A primacy code for odor identity. Nat. Commun. *8*, 1477.

Wu, A., Yu, B., Chen, Q., Matthews, G.A., Lu, C., Campbell, E., Tye, K.M., and Komiyama, T. (2020). Context-dependent plasticity of adult-born neurons regulated by cortical feedback. Sci. Adv. *6*, eabc8319.

STAR★METHODS

KEY RESOURCES TABLE

REAGENT or RESOURCE	SOURCE	IDENTIFIER
Deposited data		
Raw and analyzed simulation data	This paper	https://doi.org/10.5281/zenodo.6143717
Code for simulating and analyzing network responses	This paper	https://doi.org/10.5281/zenodo.6143717
Software and algorithms		
MATLAB_2021a	MathWorks	https://www.mathworks.com/products/matlab.html

RESOURCE AVAILABILITY

Lead contact

Further information and requests for resources and reagents should be directed to and will be fulfilled by the Lead Contact, Krishnan Padmanabhan (krishnan_padmanabhan@urmc.rochester.edu).

Materials availability

This study did not generate new unique reagents.

Data and code availability

- Simulated data have been deposited at Zenodo and are publicly available as of the date of publication. DOIs are listed in the key resources table.
- All original code has been deposited at Zenodo and is publicly available as of the date of publication. DOIs are listed in the key resources table.
- Any additional information required to reanalyze the data reported in this paper is available from the lead contact upon request.

METHOD DETAILS

Organization and architecture of the model

The MOB consisted of 50 glomeruli (G) corresponding to the olfactory receptor neuron (ORN) inputs (Mombaerts et al., 1996). Each glomerulus was connected to 25 mitral/tufted (M/T) cells for a total 1250 M/T cells. Within the MOB, a local population of 12,500 inhibitory granule cells (GCs) formed reciprocal and lateral inhibitory connections with M/T cells. Individual M/T cell ''projections'' formed random excitatory connections with 10,000 piriform cortical cells (PCs) in PCx. These PCs in turn ''projected'' back to the olfactory bulb, providing excitatory feedback (thick lines in Figure 1A) onto the inhibitory granule cells in the bulb. Within PCx, two types of inhibitory interneurons were included: a population of 1,250 feedforward inhibitory neurons (FFIs) that received excitatory input from M/T cells and inhibited both PCs and other FFIs, and a population of 1,250 local feedback inhibitory neurons (FBIs) that received input from a random subset of PCs and subsequently inhibited PCs and other FBIs.

Our model including the predominance of inhibitory granule cells (GCs) in the bulb (outnumbering M/T cells 10 to 1), the distributed connections between M/T cells and GCs (Urban and Sakmann, 2002; Willhite et al., 2006), the random projections of M/T cells to the piriform cortex (Ghosh et al., 2011; Miyamichi et al., 2011; Sosulski et al., 2011), the local inhibitory populations in the cortex (Bekkers and Suzuki, 2013; Bolding and Franks, 2018; Oswald and Urban, 2012) and the structure of feedback from the piriform cortex to the bulb (Choi et al., 2011; Padmanabhan et al., 2016; Price and Powell, 1970). Furthermore the model includes including such features as M/T biophysical diversity (STAR Methods) and glomerulus-specific long latency inhibition of granule cells (Figure S1) were matched to experimental data (Kapoor and Urban, 2006; Padmanabhan and Urban, 2014; Soucy et al., 2009).

Voltage dynamics of individual neurons

The voltage dynamics of individual cells in the network were modeled as spiking neurons (Izhikevich, 2003) described by a two-dimensional (2D) system of ordinary differential equations of the form,

$$\frac{dv}{dt} = 0.04v^2 + 5v + 140 - u + I$$
$$\frac{du}{dt} = a(bv - u) \quad \text{(Equation 1)}$$

with the after-spiking resetting

$$\text{if } v \geq 30mV, \text{ then } v \leftarrow c,\ u \leftarrow u + d \quad \text{(Equation 2)}$$

Here v represented the voltage (mV) of the neuron and u represented a dimensionless membrane recovery variable accounting for the activation or inactivation of ionic currents; t is time and has unit of ms; a,b,c and d are parameters that were be adjusted to generated diverse firing patterns; I represented synaptic currents or injected dc-currents to the neuron.

We choose to use this neuron model to simulate the voltage dynamics of individual neurons because: 1). It combined the biological plausibility of the Hodgkin–Huxley neuron model and the computational efficiency of leaky integrate-and-fire neuron model, allowing us to simulate tens of thousands of spiking neurons simultaneously in our network; 2). Different combinations of the parameter values a,b,c and d could reproduce a diversity of firing patterns of neurons of known types, so we could capture the biophysical diversity in the firing properties for different types of neurons in olfactory system, such as the mitral/tufted (M/T) cells and granule cells in the main olfactory bulb (MOB), and piriform cortical cells and other local inhibitory interneurons in piriform cortex (PCx). In order to achieve heterogeneity such that different cells within the same type exhibited different dynamics, we introduced randomness in the parameter assignment (see Table S1). The r_i was a random variable uniformly distributed on the interval $[0, 1]$ and i denoted the neuron index. For example, the parameter a was distributed on the interval $[0.02,\ 0.1]$ within which various firing patterns could emerge. We also used r_i^2 or r_i^4 to bias the distribution to different extents for different cell types. Overall, based on our choice of parameters in the Izhikevich model, the spiking patterns of PCs and M/T cells largely fell into the category of regular spiking, intrinsically bursting or chattering neurons (Connors and Gutnick, 1990; Davison and Ehlers, 2011; Padmanabhan and Urban, 2014). Inhibitory neurons including GCs and FFIs/FBIs in the network generated spiking patterns as fast spiking neurons and low-threshold spiking neurons (Burton and Urban, 2015; Egger, 2005; Gibson et al., 1999; Suzuki and Bekkers, 2012).

Within the same cell type, the parameters spanned a wide range of values to achieve heterogeneity in cell dynamics. Especially for GCs, our model did not distinguish granule cells and dSACs, and therefore GCs in our model consisted of both granule cells and dSACs.

Synaptic input I to each neuron depended on the neuron type. For a cell i in MOB, I_i was a linear superposition of various sources

$$I_i = I_i^{mc-ex} + I_i^{gc-in} + I_i^{osn} + I_i^{\text{feedback}} + \xi_i \quad \text{(Equation 3)}$$

Here, I_i^{mc-ex} represented excitation from M/T cells and existed for both M/T cells and GCs. For GCs, when an M/T cell fired, the excitatory postsynaptic current (EPSC) I_i^{mc-ex} into different GCs were delayed by different latencies, resulting in different spiking latencies of GCs (Figure S1), consistent with previous experimental findings in the olfactory bulb granule cell network (Kapoor and Urban, 2006). The I_i^{gc-in} represented inhibition from GCs and existed for both M/T cells and GCs. I_i^{osn} represented glomerular input and only existed for M/T cells. When a glomerulus was activated by a model odor, it provided correlated inputs I_i^{osn} to the M/T cells driven by that glomerulus. When a glomerulus was activated, the input current I_i^{osn} that an associated M/T cell received was modeled as a step function with Gaussian noise added (Figure S2). Since each glomerulus received inputs from a set of receptor neurons expressing the same olfactory gene type, the inputs to individual glomerulus from receptor neurons were correlated (Dhawale et al., 2010; Koulakov and Rinberg, 2011; Lledo et al., 2005; Wachowiak et al., 2004). Therefore, we assumed that the glomerular inputs to the apical dendrites received by the M/T cells associated with the same glomerulus were correlated, and the values in Figure S2 indicated the average correlation coefficient among them. No input correlation between M/T cells associated with different glomeruli was assumed. I_i^{feedback} represented excitatory centrifugal input from piriform cells and was non-zero only for GCs when feedback is ON. We set it to zero for all GCs when feedback was OFF. The ξ_i represents Gaussian white noise input with zero mean and standard deviation $\sigma = 1.75$ for M/T cells and $\sigma = 0.8$ for GCs.

Similarly, for a cell i in PCx, I_i was composed of

$$I_i = I_i^{mob} + I_i^{pc-ex} + I_i^{in} + \eta_i \quad \text{(Equation 4)}$$

where I_i^{mob} represented input from M/T cells in MOB and only existed for piriform cortical cells (PCs) and feedforward inhibitory neurons (FFIs); I_i^{pc-ex} represented excitation from PCs and existed for both PCs and feedback inhibitory neurons (FBIs); I_i^{in} represented inhibition from local inhibitory neurons including FFIs and FBIs; η_i represented Gaussian white noise input (zero mean and standard deviation $\sigma = 0.9$) and only existed for PCs.

Each action potential fired by a presynaptic neuron evoked a jump in the corresponding synaptic inputs of all its postsynaptic targets by an amount equal to the appropriate synaptic strength. For example, action potentials of an M/T cell induced jumps in the excitatory currents of their postsynaptic target neurons, including I_i^{mc-ex} in M/T cells and GCs in MOB, and I_i^{mob} in FFIs and PCs in PCx. These synaptic inputs then decayed to zero with time constant $10ms$. The height of the jump was determined by the pairwise synaptic strength between any two neurons and their values were given in the synaptic weight matrix described in the next section.

SYNAPTIC STRENGTH AND MODEL NETWORK ARCHITECTURE

The MOB consists of 50 glomeruli, each of which drives 25 M/T cells, thus a total 1250 M/T cells in MOB. A local population of 12,500 inhibitory GCs formed reciprocal and lateral inhibitory connections with M/T cells. Thus, within the MOB, we generated a weight matrix $\mathbf{W}_{mob}$ of $13,750$ by $13,750$ with entry W^{ij}_{mob} representing the synaptic strength from presynaptic neuron j to postsynaptic neuron i. Depending on the cell type, this matrix $\mathbf{W}_{mob}$ was partitioned into four sub-matrices, i.e., from M/T cell to M/T cell, from M/T cell to GC, from GC to M/T cell and from GC to GC. The specific value of each entry in $\mathbf{W}_{mob}$ was assigned randomly according to two parameters we chose for each sub-matrix. One was the connection density (the percentage of non-zero synaptic weights) and the other was the average synaptic strength (mean of a uniform distribution from which individual synaptic weights were sampled). Each sub-matrix had its own value of the connection density and average synaptic strength. In particular, the connection density and average synaptic strength between M/T cells driven by the same glomerulus were higher than between M/T cells driven by different glomeruli.

Individual M/T cell "projections" formed random excitatory connections with 10,000 PCs and 1,250 FFIs in PCx, giving rise to a feedforward weight matrix $\mathbf{W}_{ff}$ of $11,250$ by 1250. Within PCx, PCs formed recurrent excitations with each other. The FFIs inhibited both PCs and other FFIs, and another population of 1,250 FBIs that received input from a random subset of PCs inhibited PCs and other FBIs. Therefore, we generated a matrix $\mathbf{W}_{pcx}$ of $12,500$ by $12,500$ that identified all synaptic weights between cells in PCx. PCs "projected" back to the MOB, providing excitatory feedback to GCs, giving rise to a feedback weight matrix $\mathbf{W}_{fb}$ of $12,500$ by $10,000$. Under the condition of feedback OFF, this $\mathbf{W}_{fb}$ was set to be a zero matrix. The connection density and average synaptic strength for all sub-matrices can be found in Table S2. The parameters are all chosen heuristically based on previous theoretical and experimental studies listed in Table S2.

Feedback projections from piriform cortex to the bulb may be structured. Retrograde rabies tracing has demonstrated that piriform cells projecting to GC populations in the bulb tend to be spatially clustered (Padmanabhan et al., 2016). Furthermore, a number of studies suggest that GC synapses are especially sensitive to plasticity (Livneh and Mizrahi, 2012; Sailor et al., 2016), either through adult neurogenesis or more traditional mechanisms of synaptic reorganization. To implement all of these features, we structure the feedback projections to GCs such that the PCs receiving feedforward inputs from the M/T cells of certain glomeruli project back to the GCs which were reciprocally connected with M/T cells associated with other glomeruli. Reciprocal connectivity between M/T cells and GCs was defined as: M/T-1 excites GC-1 and GC-1 inhibits M/T-1, as observed by many studies (Wanner and Friedrich, 2020; Willhite et al., 2006). Across the M/T population, there were 291 ± 9 (mean $\pm$ SD, $n = 1250$ M/T cells) GCs that were reciprocally connected with each M/T cell. As a result, each PC projected to 7368 ± 64 GCs (mean $\pm$ SD, $n = 10000$ PCs) with weight magnitude larger than 0.01. All feedback synaptic weights were randomly generated with small magnitude less than 0.05, and this structure gave rise to a dense but weak connectivity matrix $\mathbf{W}_{fb}$. Due to the sparsity of the PC firing when feedback was ON, this dense and weak top-down connectivity ensured robust influence of PCs on GC activity and thus the contribution of PCx on odor processing in MOB.

Model odor definition

Model odors were defined by the combinatorial patterns of glomeruli which were activated successively with different glomerular timing, a pattern recapitulating the spatiotemporal structure of odor inputs (Rubin and Katz, 1999; Meister and Bonhoeffer, 2001). Specifically, when a model odor was presented, three glomeruli were activated (6% of all glomeruli) and all the M/T cells associated with those glomeruli received correlated glomerular input I^{osn} which lasted for 90 ms (Figures 1B and S1). We also activated 5, or 10 glomeruli, reflecting not only the combinatorics of timing and identity, but also different number of glomeruli activated by natural odors. A table of 300 model odors were defined as the odor inputs to our network Figure S1).

Model odors with denser glomerular activation

To ensure our results remain valid for models odors with denser glomerular activation and higher degree of overlap, we also generated different model odors which activated 5 or 10 glomeruli respectively (see Figures 2F and 4C), which gave rise to 10%–20% of glomerular activation, similar to the level evoked by natural odors in awake mice (Vincis et al., 2012). We also did linear decoder analysis for these model odors with higher degree of overlap. The odor pair in Figure S7F were overlapped in the first 3 glomeruli and thus highly correlated ($corr = 0.90$) and the odor pair in Figure S7G were overlapped in the first 7 glomeruli and also highly correlated ($corr = 0.91$).

Network dynamics simulation

The network dynamics were governed by a large set of differential equations of the form Equation (1) coupled by the pairwise synaptic weights between different neurons. These equations were numerically solved using the first-order Euler's method with a uniform step size $\Delta t = 1ms$. The initial conditions were obtained by first running the network without glomerular input ($I_i^{osn} = 0$) but only with noisy input (ξ_i and η_i) for $600ms$. This allowed the network to reach a steady state determined by its intrinsic dynamics. Afterward we simulated the network using model odors for $250ms$ which was roughly the duration of one sniff cycle. The network spiking activity within this period were used for later analysis.

Randomly sampled "single units" from the network

For each odor, we randomly sampled 9 cells from the entire M/T cell population, with at least 1 odor-driven M/T cell included. We then computed the population firing rate for these sampled M/T cells. This process of random sampling was repeated 20 times, with each

repeat reflecting a different random subset of 9 M/T cells to ensure that the kinetics was not a result of artifacts of selecting a single subset. The mean population firing rate of sampled M/T cells across all 20 repeats was then used to fit the exponential function for that odor (Figure 2E3). To obtain error bar for a single odor, as shown in Figures 2E1 and 2E2, the entire process was repeated 20 times so that we obtained 20 mean population firing rates, each of which was generated by 20 times of random sampling. This sampling strategy allowed us to compare our model results where we had access to every cell in the network, with experiments where a subset of neurons are recorded from using either tungsten or silicone probes (Bolding and Franks, 2018; Chockanathan et al., 2021; Rinberg et al., 2006).

Exponential fit of the kinetics of randomly sampled M/T units

We fit a single-term exponential function $y = a \cdot exp(-\tau x)$ using the Matlab code fit(x,y,'exp1'), where the coefficient τ denoted the time constant of the kinetics decay. For each odor, we fit the function from the peak of the mean firing rate to the end of the sniff and obtained time constant τ.

Balance between excitatory and inhibitory synaptic inputs

To understand the balance between excitatory and inhibitory synaptic inputs for MOB cells, we computed the overall amount of excitatory and all inhibitory inputs to each cell. The excitatory sources for M/T cells included the recurrent MC excitation I_i^{mc-ex}; for GCs they included excitation from M/T cells I_i^{mc-ex} and excitatory feedback $I_i^{feedback}$ when feedback was ON. The inhibitory source for both M/T cells and GCs was the I_i^{gc-in}. For each MOB cell, the areas under the excitatory and inhibitory synaptic inputs averaged over 10 trials were computed respectively and an algebraic sum of the two. This value, as referred to E/I balance in Figures 3C and 3D, was a measurement of the overall driving effect of the excitatory and inhibitory inputs on each cell during a sniff. Positive (negative) values for a cell indicated that it was dominated by excitation (inhibition) and a zero simply corresponded to a balance.

Principal component analysis (PCA)

Spiking activity of piriform cells (PCs) was binned into a 5*ms* sliding time window and averaged across trials (each model odor was presented in 10 trials). We then concatenated the trial-averaged responses of all piriform cell (PCs) to all 300 model odors under both conditions of feedback OFF and ON, resulting in a matrix of 10,000 PCs by 247 time bins × 300 odors × 2 conditions. Response covariance matrices (10,000 by 10,000) were computed for this concatenated matrix (after subtracting the mean responses averaged across time bins, odors, and conditions). This gave us a single set of eigenvectors, thus the same eigenspace into which PC responses for both feedback OFF and ON were projected and compared. Each 10,000-dimensional PC response vector was then projected onto the first 3 principal eigenvectors for visualization (Figure 5) and the first 50 principal eigenvectors for computations (Figures 6 and S6).

Symmetrized Kullback–Leibler divergence D_{KL}

To quantitatively assess the effect of feedback on odor processing in the PCx, we computed the instantaneous symmetrized Kullback–Leibler divergence D_{KL} of the two distributions $P_t(y|\text{Odor}-1)$ and $P_t(y|\text{Odor}-2)$ which were built from the single-trial PC responses to the two odors at each time step t. We used three types of odor pairs: 1). odor pairs with identity differences in a single glomerulus (19 pairs for glomerular-1, 11 pairs for glomerular-2 and 18 pairs for glomerular-3); 2). odor pairs with timing differences in a single glomerulus (19 pairs in G1, 11 pairs in G2 and 18 pairs in G3); 3). odor pairs with both identity and timing differences in multiple glomeruli (192 pairs in total with different correlations in latency).

For a given odor pair, each of the odors was presented for 100 trials and the responses of PCs were recorded and then projected to the first 50 principal eigenvectors. At each time step, the PC responses to each odor gave rise to a cluster of points in the 50-dimensional space, with each point in the cluster corresponding to a single-trial response. The separation between the two clusters at time t were computed using the Kullback–Leibler divergence $D_{KL}(t)$ between the distributions of the two clusters along the optimal readout dimension γ_t (Figure 6A), which was computed from multiplying the inverse covariance matrix Σ_t^{-1} (50 by 50) of the two clusters with the vector connecting the cluster means $\Delta\mu_t$ (50 by 1). We exploited the Kullback–Leibler divergence since it was a direct measurement of how one distribution was different from another and also a measurement of information gain. Note that since the PC responses evolved over time, the clusters of points and thus the optimal readout dimension γ_t (as well as Σ_t^{-1} and $\Delta\mu_t$) also varied with time. Therefore the $D_{KL}(t)$ was a function of time (Figure 6).

Standard Kullback–Leibler divergence is not symmetric and therefore depends on the order of the two distributions. To correct that, we therefore symmetrized it by computing (Masuda and Doiron, 2007)

$$D_{KL}(t) = \frac{KL_t(\text{O1}\|\text{O2})\, KL_t(\text{O2}\|\text{O1})}{KL_t(\text{O1}\|\text{O2}) + KL_t(\text{O2}\|\text{O1})} \quad \text{(Equation 5)}$$

where O1 and O2 represent Odor-1 and Odor-2, and

$$KL_t(\text{O1}\|\text{O2}) = \sum_y P_t(y|\text{Odor}-1) log \frac{P_t(y|\text{Odor}-1)}{P_t(y|\text{Odor}-2)} \quad \text{(Equation 6)}$$

is the standard Kullback–Leibler divergence between the distribution $P_t(y|\text{Odor}-1)$ and $P_t(y|\text{Odor}-2)$, which were built from those single-trial PC responses to the two odors at time step t. We computed the $D_{KL}(t)$ for feedback OFF and ON using the same procedure described above. Accumulated D_{KL} (Figures 6E–6G) was computed as the area under mean $D_{KL}(t)$ over a sniff cycle.

Time-fixed readout dimension was computed by averaging the time-varying readout dimension γ_t across time and conditions (feedback OFF and ON).

Linear decoder analysis: K nearest neighbor algorithm

The K nearest neighbor approach was used to decode odor identity from the projected ensemble responses of PCs to any given odor pair (Padmanabhan and Urban, 2010). Consistent with the computation of symmetrized Kullback–Leibler divergence D_{KL}, analysis was performed in the space of the first 50 principal components. The original data were broken up into testing and training sets. The training sets established the location of PC responses to known odors (i.e., known PC responses) in the principal component space and the testing sets were probed with respect to these known PC responses. The Euclidian distance of the unknown odors to all PC responses was then calculated and the K nearest neighbors were used to determine to which odor the unknown PC activity was responding to. This process of generating testing and training sets was repeated 30 times, with each repeat reflecting a different random population of testing and training to ensure that the decoding accuracy was not a result of artifacts of selecting a single testing/training population. Free parameters in the K nearest neighbor algorithm included the ratio of testing to training data and the number of nearest neighbors used in the calculation. For training/testing, we used ratios of 50%, 70% and 90%. We examined the algorithm's accuracy when 3, 5 and 7 nearest neighbors were used.

Sequential probability ratio test (SPRT)

To make predictions on animal's behavioral performance under the condition of feedback OFF or ON, we applied the sequential probability ratio test (Gold and Shadlen, 2007) and simulated the decision-making process of a model agent in a two-alternative forced-choice (2AFC) task. In such a task, on each trial, the model agent was presented with a randomly chosen odor (Odor-1 or Odor-2) and was required to report which odor was presented by the end of a single sniff. We chose three different model odors as the original odor (Odor-1) from the table of 300 model odors we defined. We then shifted the activation timing of a single glomerulus by $5ms$ increment/decrement in the three original odors. Therefore, the odor pairs here were composed of one original odor and its counterpart which had the timing of a single glomerulus shifted by different amount of time (Figure 7).

First, similar to the computation of $D_{KL}(t)$, for a given odor pair, each of the odors was presented for 100 trials and at each time step, the two distributions $P_t(y|\text{Odor}-1)$ and $P_t(y|\text{Odor}-2)$ were obtained from the single-trial PC responses along the optimal readout dimension. We then fit a normal distribution to the two distributions respectively and we used the same standard deviation σ in the normal distribution for both odors, which allowed us to generate samples more efficiently. According to SPRT, the agent's decision process was depicted as the accumulation of noisy momentary evidence over time until a threshold was reached, or the stimulus was extinguished. Supposing we generated a sample y^* at time step t, the momentary evidence was then computed as

$$ev(t) = log\frac{\tilde{P}_t(y^*|\text{Odor}-1)}{\tilde{P}_t(y^*|\text{Odor}-2)} \quad \text{(Equation 7)}$$

Here, $\tilde{P}_t$ denoted the fitted normal distribution. A choice was made when the accumulated evidence $\sum_t ev(t)$ reached one of the decision boundaries $\pm B_d$ (Figure 7A3) and the reaction time was recorded by adding a residual motor delay, which was normally distributed with mean $=50ms$ and SD $=5ms$. We generated 1000 samples y^* at each time step for each model agent (10 agents in total). Therefore, each agent performed 1000 trials for the same pair of odors. For each agent, we computed the accuracy as the proportion of correct choices among the 1000 trials. The average reaction time across the 1000 trials was reported as the reaction time for that agent. Parameter values used in SPRT analysis were listed in Table S3.

We set the widths of the two Gaussians in SPRT to be equal as this was the normal formalism for the SPRT. Our approach was to use the behavior model to find the upper bound of performance. Beyond this technical constraint, we also approached the problem from two empirically motivated constraints:

1) We assumed that the PCx encoded odor information, which was quantified by the KL-divergence, and the decision-making process was performed in some downstream areas, which received and accumulated evidence from PCx. The information transmission from PCx to the downstream decision-making area may have involved other sources of noise. As we could not know the structure of this noise, nor was it likely to be from a single source, i) we assumed it would have a Gaussian distribution to draw samples and ii). we assumed it to be unbiased such that noise only increased the uncertainty/width of the distribution.
2) Equal width of the distributions result in the decision-making being harder than unequal width, because when we computed the momentarya evidence, the log likelihood of a sample drawn from two Gaussian distributions with equal mean but different widths could still be large, while it would be zero if we used equal width.

These two factors allowed us to incorporate all the uncertainty between information processing in piriform cortex and decision making that likely included both sensory and motor areas; assumptions that were necessarily multiparametric and therefore modeled as Gaussian so as not to include any biases.

QUANTIFICATION AND STATISTICAL ANALYSIS

Statistical tests for significance were performed with a two-sided Wilcoxon rank-sum test (ranksum function in MATLAB) when samples were independent (Figures 5A and 5B) and with a two-sided Wilcoxon signed rank test (signrank function in MATLAB) for paired samples (Figure 2E3, 4E1, and 4E2). Correlation coefficients between two variables were computed as the Pearson correlation coefficient (corrcoef function in MATLAB). Statistical significance was defined by a p value <0.05. The statistical details (correlation coefficient, p value, sample size n) are provided in the figures, figure legends, or the text of the Results section. The specific meaning of the sample size n is clarified when used.